

PAPER • OPEN ACCESS

Validation and predictions of reduced models for stochastic electron transport in MAST and MAST-U

To cite this article: F Palermo et al 2025 Plasma Phys. Control. Fusion 67 065004

View the article online for updates and enhancements.

You may also like

- Ideal magnetohydrodynamic instabilities in tokamaks driven by strong toroidal plasma rotation: an analytical and numerical investigation C Schaumans and J P Graves
- SOLPS analysis of the MAST-U divertor with the effect of heating power and pumping on the access to detachment in the Super-x configuration E Havlíková, J Harrison, B Lipschultz et al.
- Real-time plasma equilibrium reconstruction and shape control for the MAST Upgrade tokamak
 H. Anand, W. Wehner, D. Eldon et al.

Plasma Phys. Control. Fusion 67 (2025) 065004 (20pp)



Validation and predictions of reduced models for stochastic electron transport in MAST and MAST-U

F Palermo^{1,*}, F J Casson¹, F Koechl¹, N Chulu-Chinn^{1,2}, B F McMillan², L Garzotti¹, C Angioni³ and C M Roach¹

E-mail: francesco.palermo@ukaea.uk

Received 9 January 2025, revised 28 April 2025 Accepted for publication 7 May 2025 Published 19 May 2025



Abstract

Magnetic stochastic perturbations can strongly influence cross-field transport in high β tokamak plasmas. The impact of stochastic magnetic fields on electron heat transport in MAST/MAST-U is studied over a range in collisionality. The physics guided semi-empirical Rechester-Rosenbluth and Rebut-Lallia-Walkins models are separately used to describe the stochastic field contribution to electron heat transport, and to supplement TGLF reduced model predictions of the transport from electrostatic turbulence. These combined models of anomalous transport are implemented in the JINTRAC code, and applied to transport simulations of the flat-top phase in MAST/MAST-U. The different ranges of validity of the stochastic transport models are briefly reviewed, focusing on the length-scales involved in the transport process. The principal relevant length-scales have been calculated using the plasma equilibrium characteristics, and used to determine the most appropriate stochastic transport model that is then applied in each shot. This analysis strongly suggests that stochasticity is an important transport mechanism in spherical tokamaks that should be included in ST plasma scenarios where strong electron heat transport is not described by other instabilities.

Keywords: stochastic transport, spherical tokamaks, MAST-U, electron transport, MAST, STEP

1. Introduction

Magnetic confinement fusion (MCF) research has largely focused on the design and optimisation of conventional aspect ratio tokamaks, but in parallel other configurations of devices including stellarators [1] and spherical tokamaks (STs) [2],

Original Content from this work may be used under the terms of the Creative Commons Attribution 4.0 licence. Any further distribution of this work must maintain attribution to the author(s) and the title of the work, journal citation and DOI.

have also been developed. These latter configurations could, in principle, obviate some of the engineering and more purely scientific challenges associated with delivering fusion energy from MCF devices. In fact, STs offer several practical technological advantages including: radial compactness; high effective TF coils, potentially lower cost components. From the scientific point of view, STs hold an improved plasma stability that allows operation at lower magnetic field compared to traditional tokamaks. Moreover, low aspect ratio and enhanced stability at high elongation gives STs access to operating regimes where a large fraction of the total plasma current is the self-driven bootstrap current. STs can operate at high β (where β is the ratio of plasma pressure to magnetic field energy density), and have achieved stable operation across a wide

¹ CCFE, UKAEA, Culham Campus, Abingdon OX14 3DB, United Kingdom

² University of Warwick, Coventry CV4 7AL, United Kingdom

³ Max Planck Institut für Plasmaphysik, Boltzmannstr. 2, Garching bei Munchen, 85748, Germany

^{*} Author to whom any correspondence should be addressed.

space in κ and β/l_i [3, 4], with energy confinement times that, while broadly consistent with multi-machine scaling laws, scale favourably with collisionality [5, 6].

The interest in STs has led to the construction of several machines in the past decades, including START [7], NSTX [8, 9], Pegasus [10], MAST [11], GLOBUS-M [12] and -M2 [13], MAST-U [14], ST40 [15], NSTX-U [16]. More recently, the UK has embarked on the STEP project to develop an ST-based fusion power plant (FPP) concept, with a major radius $R \approx 3.6$ and an aspect ratio $A \approx 1.8$, with the goal of operating in a fully non-inductive regime and generating net electricity with a fusion power $P_f \approx 1.5 \, \text{GW}$ [17]. The design of this reactor relies on experience gained from building and operating compact STs, such as MAST and MAST-U, that have found how challenges for STs differ from those facing conventional tokamaks.

Turbulence generally dominates transport in tokamaks, but the nature of this turbulence depends on plasma parameters and can therefore be extremely diverse. In particular, electromagnetic effects and magnetic fluctuations become more important at higher pressure gradient and at higher β values, that are more typically achieved in STs. Consequently it is to be expected that in STs, especially at high β , electrostatic turbulence will be supplemented and potentially dominated by turbulence that is electromagnetic in character.

Magnetic fluctuations can have non-negligible transport implications, and often must be accounted for in the modelling of ST plasmas. In STs the turbulence is subject to stabilising effects arising from strong toroidicity reducing the impact of bad curvature, and relatively large $E \times B$ shearing rates that act to de-correlate turbulent cells [18]. However, other kind of instabilities such as Kelvin–Helmholtz (KH) can destabilize the $E \times B$ shear [19–22] as observed in gyrokinetic simulations of plasma in ST geometry configuration [23].

In STs it is often reported that the ion heat transport is close to neoclassical level [6] (although this is relatively large compared to high performing plasmas in conventional tokamaks) and that electron heat transport dominates the heat losses. For this reason the electron heat transport channels in STs from ETG and MTM turbulence have received particular attention [18, 24–26]. Nonlinear simulations of electromagnetic turbulence have proved more challenging computationally than for electrostatic turbulence, but a few such simulations studies have been performed for ST experiments and conceptual FFPs [26–28].

Microtearing instabilities, MTM, offer one mechanism that could be responsible for electron heat transport in STs, as these saturate at large amplitudes at the lower magnetic fields in STs. MTMs are electromagnetic instabilities, and resemble high-wavenumber tearing modes [29], and are so-named because of the mode's characteristic breaking of equilibrium magnetic field lines to generate localized magnetic islands. There are several analytic theories of MTM instabilities in different regimes, but the drive mechanisms are less well validated against experiments than those associated with kinetic ballooning modes (KBM) or electrostatic instabilities. The analytic theories of MTMs generally apply in idealised regimes, and numerical investigations have proved essential

for exploring this instability in the conditions of ST experimental plasmas. Gyrokinetic studies have demonstrated that microtearing instabilities can play significant roles not only in spherical, but also in conventional aspect ratio tokamaks [27, 29–31]. Moreover, gyrokinetic simulations show that MTM is unstable over a wide range of collisional regimes [32].

The saturation of MTM turbulence and dependencies on collisionality and temperature gradient have been studied numerically in [26, 28, 33]. Depending on local equilibrium conditions, microtearing mode turbulence can be sensitive [27] or insensitive to [30] equilibrium $E \times B$ flow shear stabilisation effects, and this may be due to differences in magnetic shear [34, 35]. These subtle influences on the saturation of microtearing modes are probably related to a global stochastic behaviour of the magnetic field lines, and have an important impact on the associated transport. Owing to the rapid parallel streaming of electrons, reduced models of stochastic transport traditionally focussed solely on the transport of electron heat, which is consistent with findings from gyrokinetic calculations of MTM turbulence in STs [26, 27]. We note, however, that there is evidence from experiments with ambient stochastic field regions in stellarators [36] and in tokamaks with externally imposed resonant perturbations [37], that stochasticity static relative to the turbulence can also induce particle and momentum transport; theory has recently been developed to understand this [39]. This paper concerns turbulent (i.e. not ambient) stochastic fields in the core of tokamaks, however, and uses models where electron heat is the dominant and only stochastic transport channel. Reduced models for the core transport from MTM turbulence are required for integrated transport scenario modelling, but are not yet highly developed or validated against experiments. Previous transport simulations applying the reduced core transport model TGLF [40]⁴ to MAST and NSTX discharges, underestimated the electron transport to varying degrees, indicating that other transport mechanisms may be playing an important role in electron heat transport [41].

In a recent extension of previous studies, transport simulations using the TGLF model and NEO for the neoclassical transport were found to be consistent with experimental data from two NSTX discharges dominated by electrostatic turbulence, one in L-mode and one in H-mode [42].

It is important to note that there is no exhaustive theory to describe turbulent diffusion of plasma in a stochastic magnetic field. This problem involves the interaction of different scales in turbulent transport and represents a very fascinating subject in plasma physics. Magnetic reconnection can be driven by large-scale and micro-scale physics over a broad range of timescales, and the resulting stochastic fields can affect the transport evolution of global plasma equilibrium profiles. This complex picture has been approached by different reduced models among which one of the most important

⁴ While the TGLF model includes magnetic fluctuations, the model was developed to describe turbulent transport from electrostatic turbulence, which dominates transport in the gyrokinetic simulations upon model is based. TGLF does not capture transport from MTM turbulence.

has been developed by Rechester and Rosenbluth (RR) to capture the essential physics [43, 44]. Other approximate theoretical and semi-theoretical models, such as those due to Rafiq [45, 46], Rebut-Lallia-Watkins [47], Hamed *et al* [48] have been developed. A robust test of the stochastic transport models against a large common dataset would be highly desirable, but this does not yet exist. An interesting recent analysis of a database of JET discarges finds support for non-diffusive transport [49], that is challenging for local transport models.

To date these reduced stochastic models have been used to predict transport in a very modest number of ST discharges, and most publications have tested only a single model. Stochastic electron heat transport from MTM turbulence has been estimated for an NSTX discharge in [50], using an empirical modification of the RR model that includes an impact of the density gradient. The role of density gradient is still not clear in stochastic theory applied to tokamaks. The normalised density gradient scale-length, R/L_n , is included in the RLW model, and gave reasonable matches to $T_{\rm exp}$ at radii and times where gyrokinetic calculations predict unstable MTMs [51] for NSTX shots. It has more recently been reported that including a model for stochastic transport from MTMs in the multimode model improves transport predictions for a high collisionality NSTX discharge [46].

A high-fidelity reduced model for core transport from MTM turbulence is needed to complement models for other classes of turbulence. One of the main goals of this paper is to provide a more complete transport model for use in the integrated modeling tools widely used for tokamak scenario prediction, like JINTRAC [52] and ASTRA [53]. In this work we implement reduced models of stochastic field transport in JINTRAC to supplement the transport from TGLF. While TGLF may be used in electrostatic or electromagnetic mode, in electromagnetic mode it has insufficient radial resolution to capture MTMs. Reduced models for MTM transport have been implemented in the code by making few physical assumptions. In particular, on the basis of theoretical and numerical works [54, 55], magnetic fluctuations $\delta B/B$ have been related to equilibrium parameters such as the temperature gradient. A similar approach has been used to select the most appropriate collisionality regime to use in the RR model. In the RLW model, transport just above the threshold critical temperature gradient for the onset of stochastic transport, is modelled using a hyperbolic tangent instead of the original Heaviside function, in order to improve the numerical stability. Transport calculations with these more complete TGLF+stochastic models are performed to predict equilibrium ion and electron temperature profiles. These predictions are then compared with measured profiles in the flat-top phase of experimental discharges from MAST/MAST-U.

The rest of this paper is structured as follows. In section 2 we describe the physics basis of reduced models of stochastic transport, emphasizing main model assumptions and regimes of validity. Brief descriptions of the JINTRAC transport suite and the reduced transport model, TGLF, follow in sections 3 and 4, respectively. Then section 5 describes the MAST/MAST-U discharges selected for transport analysis, and section 6 compares transport model predictions for

these discharges against the experimentally measured profiles. Finally the conclusions are developed in section 7.

2. Stochastic models

Perturbations of the magnetic field can have a big impact on transport processes in tokamak devices, and affect the plasma equilibrium and its evolution. If the magnetic perturbations involve reconnection and are sufficiently strong, they destroy magnetic flux surfaces and can generate stochastic magnetic field regions. The locus of points at the intersection of the magnetic field with a poloidal cross-section of the plasma is no longer a smoothly defined curve belonging to a particular magnetic surface, but becomes an area-filling set of irregular random points. The magnetic field becomes stochastic at the surface q = m/n (where m and n are integer poloidal and toroidal mode numbers) when width of the locally resonant magnetic island, w_i given by [56]:

$$w_i = 4 \left(\frac{\delta B}{B_0} \frac{r}{n} \frac{1}{\mathrm{d}q/\mathrm{d}r} \right)^{1/2} \tag{1}$$

exceeds the distance between rational surfaces, $\delta r_{\rm res}$:

$$\delta r_{\rm res} = \frac{1}{n dq/dr}.$$
 (2)

The stochasticity condition, $w_i > \delta r_{res}(r)$, requires:

$$\frac{\delta B}{B_0} > \frac{1}{4^2} \frac{r}{R} \frac{1}{q^2} \frac{1}{ns} \tag{3}$$

where safety factor $q \sim rB_0/RB_\theta$ and magnetic shear $s = r/q \, dq/dr$. The stochasticity threshold in equation (3) is exceeded at a critical mode amplitude that depends on toroidal mode number, safety factor, and magnetic shear. The relative amplitude of magnetic fluctuations, $\delta B/B_0$, increases with β , and this is often sufficiently large in STs to exceed the stochasticity threshold.

Different reduced models have been developed to describe stochasticity, though this is a complicated problem that is far from fully understood. The basic assumption is to consider an equilibrium magnetic field $\mathbf{B_0}$ perturbed through a radial stochastic displacement δx in the direction perpendicular to $\mathbf{B_0}$ corresponding to a magnetic field perturbation of amplitude δB . The equation of the perturbed field line relates δx to the parallel length, $l_{||p}$, of the perturbation in the $\mathbf{B_0}$ direction:

$$\frac{\delta x}{l_{||p}} = \frac{\delta B}{B_0}. (4)$$

By assuming that $l_{||p}$ length is travelled with a ν velocity in a time $\delta t = l_{||p}/\nu$ we can write for the diffusion coefficient along the perpendicular direction:

$$D_{\text{eff}} = \frac{\delta x^2}{\delta t} = \left(\frac{\delta B}{B_0}\right)^2 l_{||p} v = D_m v \tag{5}$$

where D_m is the magnetic diffusion coefficient that has the dimension of a length. The D_m coefficient provides a

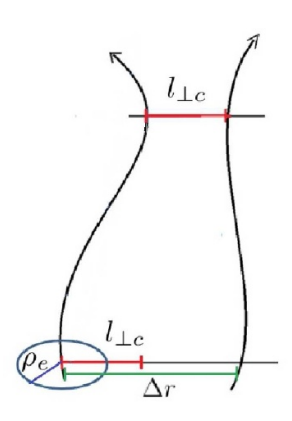


Figure 1. Stochastic perturbed magnetic field lines that approach each other at a decorrelation distance $l_{\perp c}$ generally of the order of the electron Larmor radius ρ_e allowing an electron the possibility to jump from one line to another line via collisional process. The maximum distance between the magnetic field line is represented by Δr .

measure of the stochastic behaviour of the magnetic field via the unknown longitudinal length scale $l_{||p}$. The quantity v in equation (5) is a characteristic velocity associated to the event. This velocity could be, for example, the velocity of an electron that moves along the magnetic field with a gyroradius equal to ρ_e . This latter parameter, as discussed in section 3.1, plays via its dependency on temperature and magnetic field an important role in setting magnetic fluctuations. Thus, it is not difficult to understand dependency of $\delta B/B$ on the $\beta = n(T_e + T_i)/(B^2/2\mu_0)$ value. Finally, it is important to observe that a plasma consists of many particles and exhibits a collective behaviour, so it is important to generalize these considerations by taking a statistical approach.

2.1. Kadomsev and Pogutse model

By considering collisional effects in the framework of a diffusive plasma, Kadomsev and Pogutse in [57] developed a model able to describe the stochastic dynamics establishing a relation between the perpendicular direction characterized by a collision decorrelation length and the parallel z direction with a $D_{||}$ diffusivity. This model can be introduced by defining $l_{\perp c}$ as the perpendicular displacement required for a particle to transfer to an uncorrelated field line. In the decorrelation time δt_{\perp} required for this transition, the particles diffuses along the longitudinal direction over a length $l_{||} = \sqrt{D_{||} \delta t_{\perp}}$.

Figure 1 illustrates this mechanism whereby a particle trajectory transfers from one perturbed field line to an uncorrelated one when the perpendicular displacement from the initial field-line exceeds $l_{\perp c}$. The circle in figure 1 represents the Larmor orbit of an electron of radius ρ_e . In this model $\rho_e = O(l_{\perp c}) \ll \Delta r$, where Δr is the maximum separation between the distinct field lines. Defining a transverse diffusion coefficient $D_{\perp} = l_{\perp c}^2/\delta t_{\perp}$, allows the decorrelation

time to be expressed:

$$\delta t_{\perp} = \frac{l_{\perp c}^2}{D_{\perp}}.\tag{6}$$

Substituting for the decorrelation time into the parallel diffusion equation, $l_{||} = \sqrt{D_{||}\delta t_{\perp}}$, gives:

$$l_{||} = \left(\frac{D_{||}}{D_{\perp}}\right)^{1/2} l_{\perp c}.\tag{7}$$

Now the effective velocity of particles parallel to the magnetic field $v = l_{||}/\delta t_{\perp}$, can be expressed using (7) as:

$$v = \frac{\sqrt{D_{||}D_{\perp}}}{l_{\perp c}} \tag{8}$$

and the collective diffusive process for a collisional plasma by substituting equation (8) into equation (5) to obtain:

$$D_{\rm eff} = D_m v = D_m \frac{\left(D_{||} D_{\perp}\right)^{1/2}}{l_{|c}}.$$
 (9)

This formula describes collisional particle motion in terms of diffusion both parallel and perpendicular to the perturbed field, and particles transfer to uncorrelated field lines when the perpendicular displacement exceeds $l_{\perp c}$; this dynamics gives rise to anomalous transport in the radial direction. The model is 'collisional' in the sense that the perpendicular displacement of particles, between distinct magnetic field lines, is assumed to be completely due to collisional processes. However, in stochastic magnetic fields, collisions are not the only process that contribute to the radial transport.

2.2. Rechester-Rosenbluth model

In the same year as [57], Rechester and Rosenbluth described an alternative more efficient decorrelation mechanism [43, 44]. RR highlighted that in a stochastic field, two neighboring magnetic field lines separated by a perpendicular distance x_d , at one location, become exponentially separated on advancing in the direction of the magnetic field; i.e. the separation between particles, x(t), following field-lines initially separated by x_d , increases with the parallel displacement z(t) according to:

$$x(t) = x_d e^{z(t)/l_K} \tag{10}$$

where l_K , the Kolmogorov length scale, is an important parameter characterizing the chaotic motion of the magnetic field. This scale contains 'information' associated with the trajectories of the system, and is related to the dynamic entropy [58, 59]. The Kolmogorov statistical approach is adopted and extended by RR to a deterministic stochastically unstable system in which l_K is determined also from the geometrical configuration of the magnetic field; in tokamaks the field geometry

is characterised by the magnetic shear, which changes in the radial direction. In the Rechester-Rosenbluth mechanism the decorrelation of the magnetic field experienced by a particle, arises primarily because of the divergence of the magnetic field lines, with collisions playing a modest but yet essential role in seeding the process.

Consider field lines passing through a small circular area $A=\pi x_d^2$ of radius x_d in the poloidal plane of a tokamak plasma. The fields passing through the circle at z=0 diverge and the outer radius of the locus of the field lines increases as $x(z)=x_de^{z/l_K}$ from equation (10). From conservation of magnetic flux it follows that as the fields expand, this locus must also develop increasingly fine scale dendritic structures (of width $\delta \sim x_de^{-z/l_K}$) in the perpendicular plane as z increases. We apply this argument to field lines bounded at z=0 by a circle of radius $l_{\perp c}$, where $l_{\perp c}$ characterises the field decorrelation distance, to find that the separation between uncorrelated fields, $r_c(z)$, narrows with z as:

$$r_c(z) = l_{\perp c} e^{-z/l_K}.$$
 (11)

Assuming collisional particle trajectories governed by parallel and perpendicular diffusion:

$$r = \sqrt{D_{\perp}t} \qquad z = \sqrt{D_{\parallel}t} \tag{12}$$

it follows that:

$$r = \sqrt{\frac{D_{\perp}}{D_{\parallel}}} z. \tag{13}$$

In the limit where stochasticity plays no role, i.e. $l_K = \infty$, the decorrelation length $l_{\perp c}$ is accessed through collisions alone. Setting $r(l_{\parallel c}) = l_{\perp c}$ using equation 13. directly gives the Kadomtsev and Pogutse result of equation (6), $l_{\parallel c} = l_{\perp c} \sqrt{D_{\parallel}/D_{\perp}}$ [60].

Now let us consider an element of plasma of perpendicular thickness δ in a stochastic magnetic field. The collisional particle trajectories are governed by equation (13), and follow correlated fields described in equation (11). At increasing z the element thickness, δ , of the correlated plasma is simultaneously subjected to narrowing by stochasticity and to expansion from particle collisions, so that:

$$\frac{\mathrm{d}\delta}{\mathrm{d}z} = -\frac{\delta}{l_K} + \sqrt{\frac{D_\perp}{D_\parallel}}.\tag{14}$$

The typical thickness of this correlated region of plasma is estimated from when these opposing influences balance; i.e. when $\frac{d\delta}{dz} = 0$ at:

$$\delta = l_K \sqrt{\frac{D_\perp}{D_\parallel}}. (15)$$

Now $\delta = r_c(l_{\parallel c})$, so we obtain the parallel correlation length $l_{\parallel c}$ by combining equation (11) and equation (15) to give:

$$l_{\parallel c} = l_K \ln \left[\frac{l_{\perp c}}{l_K} \sqrt{\frac{D_{\parallel}}{D_{\perp}}} \right]. \tag{16}$$

This gives all the information required to determine the stochastic diffusion coefficient from equation (5). The characteristic velocity, $v = D_{\parallel}/l_{\parallel c}$ arises from parallel diffusion (and is obtained using $v = l_{\parallel c}/\delta t$ together with $D_{\parallel} = l_{\parallel c}^2/\delta t$). From equation (5) we have:

$$D_{\text{eff}} = D_m v = \left(\frac{\delta B}{B}\right)^2 \frac{l_{\parallel p}}{l_{\parallel c}} D_{\parallel}. \tag{17}$$

Substituting equation (16) into equation (17) gives the general expression for the RR model transport diffusivity. In section 3.1. Equation (17) will be used as the basis of RR-based models in collisional and collisionless limits in JETTO.

The RR model establishes different scales that are fundamental to stochastic transport (e.g. $l_{\parallel c}$, $l_{\perp c}$ $l_{\parallel p}$, and l_{K}) but does not quantify all of them, which is the price paid for the RR model's simplified description of stochastic transport. Appropriate models are needed to independently estimate these scales from the characteristics of the plasma configuration, and this represents the main difficulty in exploiting the model.

2.3. Rebut-Lallia-Watkins model

As discussed in section 2, if magnetic islands are sufficiently large to overlap they generate stochastic, or ergodic, magnetic field regions. The Rebut-Lallia-Watkins (RLW) model [47] is a semi-empirical description of plasma transport under such conditions, and its model predictions have been compared with measured profiles from an NSTX H-mode plasma [51].

The RLW model is based on dimensionless plasma parameters, and was first developed to predict plasma profiles in ohmic and L-mode JET discharges by exploiting an analogy between fluid and plasma turbulence. In fluids the dimensionless Reynolds number R_e , which characterizes the relative importance of momentum transport by convection and by viscous diffusion, allows to fix the transition from the laminar to the turbulence regime when R_e exceeds a critical value, $R_{e,c}$. The corresponding change in radial heat and particle flows observed in fluids is also observed in tokamaks by considering this latter as an open thermodynamic system in which heat flow could influence its stability. Thus, the RLW model determines a critical temperature gradient $|\nabla T_e|_c$ for a plasma, equivalent to a critical Reynolds number to define the development of turbulence due to a stochastic instability in a tokamak:

$$|\nabla T_e|_c = \left|\frac{\mathrm{d}T_e}{\mathrm{d}r}\right|_c = 0.06 \frac{e}{(\mu_0 m_e^{0.5})^{0.5}} \frac{1}{q} \left(\frac{\eta J B^3}{n_e T_e^{0.5}}\right)^{0.5}$$
 (18)

where η is the Spitzer resistivity and J is the current density. When the electron temperature gradient exceeds $|\nabla T_e|_c$ the electron transport becomes:

$$\chi_{\text{RLW}} = 0.5c^2 \sqrt{\mu_0 m_i} \frac{(1 - \sqrt{r/R})}{BR^{0.5}} \left(\frac{T_e}{T_i}\right)^{0.5}$$

$$\times \left(\frac{1}{T_e} \frac{dT_e}{dr} + 2\frac{1}{n_e} \frac{dn_e}{dr}\right) \frac{q^2}{dq/dr}$$

$$\times \sqrt{1 + Z_{\text{eff}}} \left(1 - \frac{|\nabla T_e|_c}{|\nabla T_e|}\right)$$

$$\times H(|\nabla T_e| - |\nabla T_e|_c) H\left(\frac{dq}{dr}\right)$$
(19)

where the Heaviside functions, denoted H(...), trigger anomalous transport above the critical electron temperature gradient in regions with dq/dr > 0. The RLW model is also sensitive to the density gradient; indeed while the model only triggers transport above a threshold in ∇T_e , the ensuing transport is twice as sensitive to the logarithmic density gradient as to the logarithmic electron temperature gradient. (This transport sensitivity to density gradient is not present in the RR models of stochastic transport discussed above.) Although the modelled microtearing transport level in equation (19) is strongly dependent on n_e , T_e , T_i , q, and their gradients, there is no clear dependence on either collisionality or β_e which should also influence microtearing-induced transport. Some of these dependences are implicitly in the critical gradient of equation (18), but this has virtually no effect on transport when the temperature gradient exceeds the critical threshold across the radial cross-section (as for the NSTX shot analysed in [51])⁵.

All of the models for stochastic field transport described in section 2 have been implemented in the integrated modelling tool JINTRAC. Transport calculations using these stochastic transport models, together with models like TGLF to describe the transport from electrostatic turbulence, to test and validate these models against experimental data from MAST and MAST-U, will be reported in section 6.

3. JINTRAC code

JINTRAC [52] is a popular transport simulation tool used by the fusion community to model and optimize tokamak plasma scenarios, and to make predictions for future devices. It incorporates a wide range of physics-modules to model different aspects of the tokamak plasma discharge, and the various modules can be selected and configured via a convenient bespoke JAMS interface. This is extremely flexible and facilitates a wide range of simulations with different levels of complexity and fidelity.

Here we exploit JETTO, the core transport solver at the heart of JINTRAC, to model the transport evolution of fixed-boundary plasma equilibria. JETTO solves the plasma fluid transport equations for quantities that are averaged over magnetic surfaces⁶, and requires the 2D plasma equilibrium for a prescribed boundary in the poloidal plane. The 2D equilibrium is either computed self-consistently using JINTRAC's internal equilibrium module ESCO, or taken from an external calculation. JETTO can be used to model a wide variety of tokamak transport problems of interest.

The transport matrix contains the various contributions to the fluxes of heat and particles, and its coefficients must be calculated for each species. This contains contributions from both neoclassical and anomalous transport. The neoclassical transport contribution is calculated independently using the NCLASS module and this is added to the anomalous transport. Calculation of the various transport coefficients requires as inputs: density, temperature, momentum and the gradients of these quantities for electrons and all ion species, and the Grad-Shafranov equilibrium (which includes the magnetic shear and q profiles). The transport models are computed within JETTO at each time step to obtain the transport matrix, and the profiles are evolved forwards in time by inverting a matrix equation [61].

Different anomalous transport models are available in JETTO such as Bohm/gyroBohm [62] and TGLF [40, 63, 64]. The latter will be used in this paper's simulations. We will additionally include the RR and RLW models of transport from stochastic magnetic fields, and we will specify regions of validity for the RR models.

3.1. Implementation of the reduced stochastic models in JINTRAC

In order to implement stochastic models in JINTRAC, different assumptions and approximations have been done. For convenience we rewrite equation (17) to make the magnetic diffusivity dependence on $\delta B/B_0$ explicit:

$$D_{\text{eff}} = D_m \frac{D_{||}}{l_{||c}} = \left(\frac{\delta B}{B_0}\right)^2 l_{||p} \frac{D_{||}}{l_{||c}}.$$
 (20)

Nonlinear drift-kinetic theory of the stochastic turbulence suggests saturation occurs at amplitude [54]

$$\frac{\delta B}{B} = \frac{\rho_e}{L_T} \tag{21}$$

where ρ_e is the thermal electron gyroradius and L_T is the electron temperature gradient scale length. Equation (21) has been obtained in [54] in the framework of a drift-kinetic theory. While gyrokinetic simulations of MTM turbulence performed with GENE at conventional aspect ratio [30, 55] and with GYRO and CGYRO for STs [26, 33], are broadly consistent

 $^{^5}$ RLW model predicted T_e profiles were reported in [51] to be in good agreement with measurements from an NSTX discharge at times when gyrokinetic simulations revealed MTMs to be unstable and dominant, but less well for times when MTMs were stable or sub-dominant.

⁶ JETTO solves 1*D* transport equations for the plasma radial profiles together with a 2*D* equilibrium equation, following the standard 1.5*D* approach to model transport in tokamaks.

with equation (21) across a range of parameters, $\delta B/B$ is also strongly sensitive to other plasma parameters including β_e , ν_{ei} , flow shear, and other equilibrium quantities [26, 33].

There are several possible approaches to improve on $\delta B/B$ from equation (21):

- more detailed reduced models for $\delta B/B$ may emerge from nonlinear gyrokinetic simulations;
- Rafiq's reduced model of stochastic transport from MTMs [45] estimates $\delta B/B$ from a nonlinear dispersion relation in simplified geometry that is independent of equation (21);
- the TGLF model can provide an estimate of $\delta B/B$ (though TGLF does not reliably capture MTMs).

Thus, further works are required to assess the sensitivity of predictions to the model input parameters, with particular attention in comparing alternative approaches to modelling $\delta B/B$. Length-scale parameters $l_{||p}$ and $l_{||c}$ are also required in equation (20). We assume $l_{||p}$ to be of the order of the major radius, R, of the tokamak [27, 50], and estimate $l_{||c}$ from experimental conditions using the analytic formula of equation (27) as discussed in section 6.

Thermal conduction coefficients come from kinetic theory, which gives $D_{||}^{e,i} \sim \chi_{||}^{e,i} \propto T_{e,i} \tau_{e,i} / m_e$ where $\tau_{e,i}$ is the electron/ion collision time, and $D_{\perp}^{e,i} \sim \chi_{\perp}^{e,i} \propto T_{e,i} / m_{e,i} \omega_{e,i}^2 \tau_{e,i}$ where $\omega_{e,i}$ is the electron/ion gyrofrequency for species e,i along parallel and perpendicular direction respectively. Thus, we can write for electrons:

$$D_{||}^{e} \sim \chi_{||}^{e} = 3.16 \frac{T_e \tau_e}{m_e} \sim v_e^2 \tau_{ei} \sim \frac{v_e^2}{\nu_{ei}}.$$
 (22)

We assume the following expression for the electron—ion collision time:

$$\tau_{ei} = 2\pi \frac{\epsilon_0^2 m_e^{0.5} (k_B T_e)^{3/2}}{Z_{\text{eff}}^2 n_i e^4 \ln \Lambda}.$$
 (23)

where ϵ_0 is the electric susceptibility and $\ln \Lambda$ is the Coulomb logarithm. By observing that $v_e^2 \tau_{ei} \sim v_e^2 / \nu_{ei} \sim v_e \lambda_{\rm mfp}$, equation (20) becomes:

$$\chi_{e_{\rm RR_{coll}}} \approx \left(\frac{\rho_e}{L_{T_e}}\right)^2 R \nu_e \frac{\lambda_{\rm mfp}}{l_{||c}}.$$
(24)

This equation has been adopted as collisional model of the RR theory. In [43] it is emphasized that equation (24) works well when $l_{||c} > \lambda_{\rm mfp}$. Then, equation (24) predicts a transport that is more or less $\lambda_{\rm mfp}/l_{||c}$ time larger than that one of the collisionless regimes. For collisionless model we have:

$$\chi_{e_{\text{RR}_{c-less}}} \approx \left(\frac{\rho_e}{L_{T_e}}\right)^2 R v_e 2 \sqrt{\frac{2}{\pi}} \left(1 - \sqrt{\frac{r}{R}}\right)$$
(25)

where the last right term is a parameter related to the fraction of passing particles [65, 66]. The adoption of f_p is also supported by gyrokinetic simulations devoted to investigate stochastic regime [67].

Concerning the RLW model, in JETTO the Heaviside function of temperature gradient that appears in the RLW heat diffusivity of equation (19), is replaced with:

$$H(|\nabla T_e| - |\nabla T_e|_c) = \frac{1}{2} \left[\tanh \left(\frac{|\nabla T_e(r)|}{b|\nabla T_e(r)|_c} - \frac{a}{b} \right) + 1 \right]$$
(26)

where a = 0.9 and b = 0.01 are parameters in a hyperbolic tangent representation of the Heaviside function that regulate the position of the critical gradient and its steepness on threshold. This smoothed representation improves numerical stability with respect to discontinuous changes in time of transport close to threshold.

4. TGLF code

The trapped-gyro-Landau-fluid (TGLF) code is a firstprinciples-based quasi-linear reduced core transport model that was developed to describe anomalous transport from predominantly electrostatic turbulence. TGLF solves linearised gyrofluid equations that account for kinetic effects including Landau damping, gyro-averaging, electron-ion collisions, impurities, trapping and other toroidal geometry effects. TGLF describes turbulent transport from various classes of microinstabilities including ion temperature gradient modes (ITG), electron temperature gradient modes (ETGs), and trapped electron modes (TEMs). TGLF calculates magnetic fluctuations so can also compute the linear properties of electromagnetic modes like KBMs and Alfvénic ITG modes, that may be important for transport in higher β regimes. Physics properties of the dominant linear eigenmodes are calculated by TGLF's gyro-fluid solver, and this is supplemented by saturation rules to set the model transport fluxes. These saturation rules were tuned to fit turbulent fluxes from databases of nonlinear gyrokinetic simulations across a wide range of plasma conditions. Several different saturation rules have been developed and released as this database has expanded: SAT0 [40], SAT1 [68], SAT2 [69], and SAT3 [70].

While TGLF captures some electromagnetic modes linearly, its saturation models (which is obviously critical to transport prediction) are tuned to gyrokinetic simulations of predominantly electrostatic turbulence. Moreover, the basis functions do not easily support the resolution required to resolve MTM. TGLF has been used routinely to model anomalous transport in conventional aspect ratio tokamaks like JET and DIII-D, including high β_p steady state plasma scenarios [71–73].

TGLF can describe transport contributions from electrostatic turbulence in STs, and there have been several comparisons of TGLF predictions against data from ST discharges [42, 74]. We note that first transport simulations for NSTX [42] using NEO for the neoclassical fluxes together with TGLF(SAT1) are found to be more stable than those using those using NEO with TGLF(SAT2), and that TGLF(SAT2) simulations for an NSTX H-mode were found to over-predict the contribution of low-*k* modes to the total turbulent flux whilst those using TGLF(SAT1) were consistent with power balance analysis [42]. TGLF does not capture MTMs, and

no saturation model has been developed in TGLF to describe transport from stochastic fields.

This is addressed here by supplementing TGLF with other models to describe the missing transport from stochastic magnetic fields. In this work TGLF is mainly run with the SAT1 and SAT2 saturation rules⁷, and the anomalous fluxes are supplemented using the reduced models of stochastic field transport described in section 2.

5. Experimental data selection and data analysis

In this work stochastic models have been supplemented with TGLF, for the first time, to make transport predictions for MAST and MAST-U plasmas. This section discusses the selection of shots for this analysis. Key parameters for MAST and MAST-U are: major radius R=0.85m, minor radius $a=0.65\,\mathrm{m}$, plasma current $I_{P_M}, I_{P_{MU}} \leqslant 1.3, 2\mathrm{MA}$, magnetic field $B_M, B_{MU} \leqslant 0.52, 0.75\,\mathrm{T}$ and pulse length $T_{P_M}, T_{P_{MU}} \leqslant 0.6, 5\,\mathrm{s}$. Where quantities differ between these devices, these are distinguished using the subscripts M and MU. Longer pulse lengths should give MAST-U longer and steadier flat-top phases than were accessible in MAST. We also note that at constant pressure, the lower magnetic field in MAST increases β and the likely impacts of transport from stochastic fields.

Transport analysis and model validation is more robust when it is applied using data to steady state shots that are MHD stable. This first analysis focuses on a small number of such discharges, but after verifying this approach it can be extended to a broader database of discharges in future work. We have selected experimental discharges, where the variation in time on temperature and density at $\rho_n = 0.5$ in the middle of the radial domain (which we label g) is characterized by $G = 1/g(dg/dt) < 3s^{-1}$. We have applied this selection criterion to high fidelity interpretive TRANSP simulations from MAST and MAST-U to find the most suitable discharges that are analysed in this paper. Four discharges that survive these selection criteria will be used in this paper at particular times, and these are: #22664, #22769 from MAST; and #46978, #47003 from MAST-U. We have also required that thermal transport is not strongly affected by Magnetohydrodynamic (MHD) instabilities in the period of interest. To illustrate this, figure 2 shows the time evolution of $\frac{1}{g} \frac{dg}{dt}$ for MAST-U#47003, and figure 3 shows the corresponding profile measurements and the TRANSP fits that were used. In particular, figure shows profiles of electron temperature (red colour), ion temperature (blue colour) and density (green colour) at t = 0.451 s. In the same way, figures 4–6 show profile comparison between experiments and TRANSP fits for shots #46978 MAST-U at t = 0.615 s, #22664 MAST at t = 0.230 s and #22769 MAST at t = 0.2 s respectively.

The radial profiles have been measured by using different diagnostic systems. The electron plasma temperature and

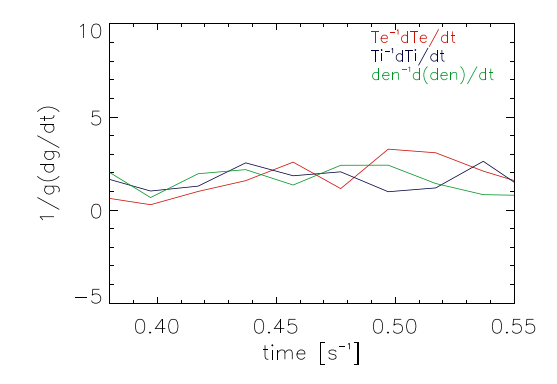


Figure 2. Time evolution of G = 1/g(dg/dt) quantity that represents the average along the radial domain for electron (red), ion (blue) temperature and density (green) profiles for the MAST-U case 47 003.

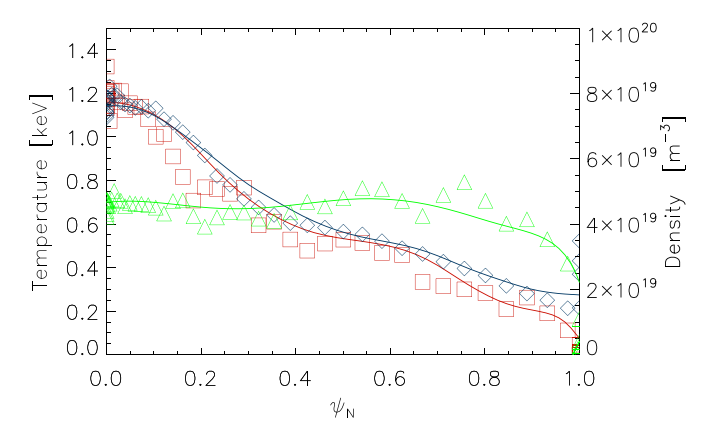


Figure 3. Comparison of density (green), electron (red), ion (blue) temperature profiles between experimental and interpretative TRANSP fit at the selected time t = 0.451 s in the flat-top phase for the MAST-U case #47003.

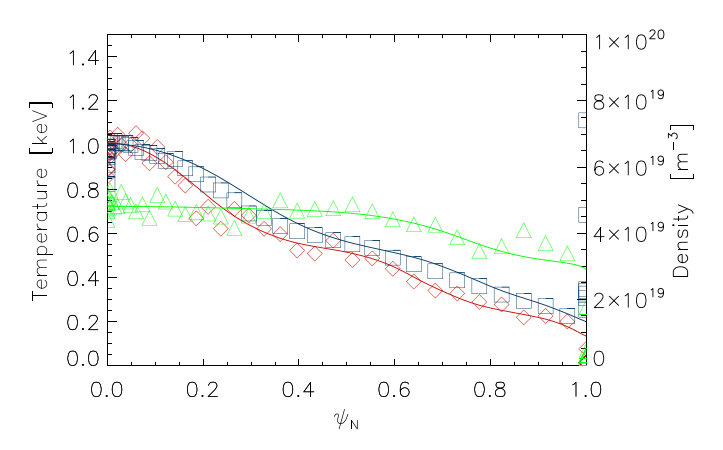


Figure 4. Comparison of density (green), electron (red), ion (blue) temperature profiles between experimental and interpretative TRANSP fit at the selected time t = 0.615 s in the flat-top phase for the MAST-U case #46978.

electron density have been obtained using the Thomson scattering system, which measures from the high field side to the low field side, along the plasma midplane. The toroidal rotation profiles have been determined by Charge Exchange

⁷ SAT1, described in [68], replaces flow shear quench rule of SAT0 [40] with a spectral shift model and accommodates findings from the first multi-scale gyrokinetic simulations, while SAT2 [69] refines SAT1 to accommodate more detailed analysis of spectra from nonlinear GK simulations.

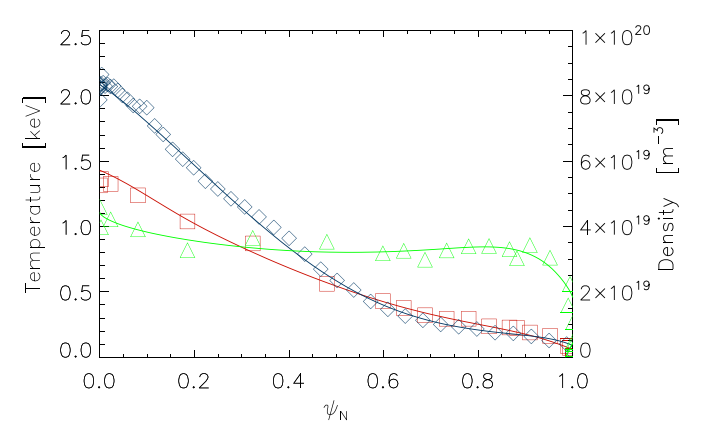


Figure 5. Comparison of density (green), electron (red), ion (blue) temperature profiles between experimental and interpretative TRANSP fit at the selected time t = 0.23 s in the flat-top phase for the MAST case #22664.

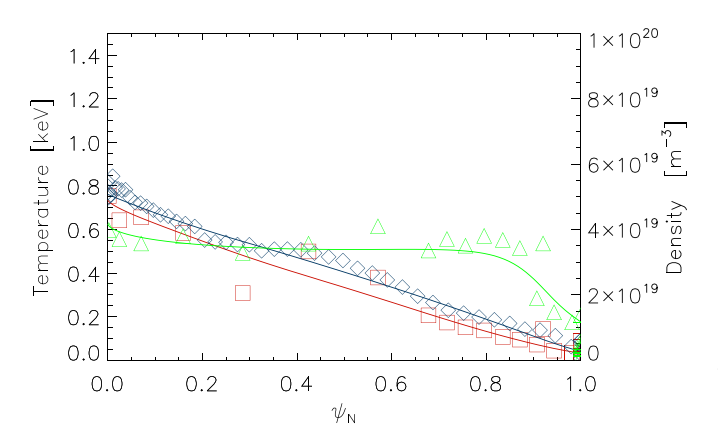


Figure 6. Comparison of density (green), electron (red), ion (blue) temperature profiles between experimental and interpretative TRANSP fit at the selected time t = 0.2 s in the flat-top phase for the MAST case #22769.

Recombination Spectroscopy, and the impurity concentration was estimated by the effective plasma charge ($Z_{\rm eff}$). Radiated power profiles have been measured by the bolometer diagnostic.

All the kinetic and MHD equilibrium reconstruction have been obtained through running TRANSP [40, 75] and EFIT [76, 77] integrated workflows using the OMFIT [78, 79] framework. The magnetic equilibrium configurations are shown in figure 7, where from left to right there is a clear gradual increase in the elongation from $\kappa=1.73$ to $\kappa=2.15$. Safety factor profiles are plotted in figure 8. Although the case 22664 presents a safety factor value close to q=1, within the limit of measurements, in all selected shots, the minimum safety factor has been maintained above unity. In agreement with this fact, no periodic MHD activity (from measurement by Mirnov coils) correlated with equilibrium quantity variations related to the presence of sawtooth, fishbones phenomena, has been detected. Values of elongation and q are

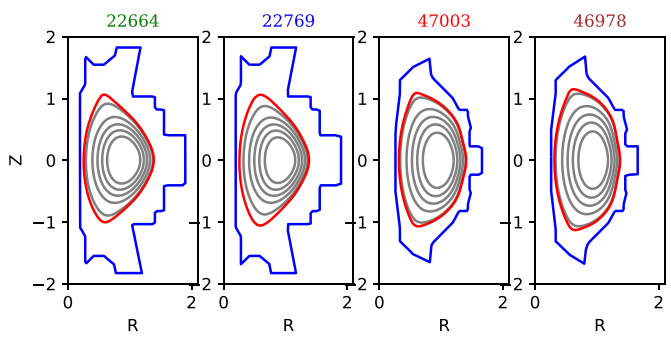


Figure 7. Magnetic configuration for MAST cases 22664 (t = 0.23 s) and 22769 (t = 0.2 s) and MAST-U cases 47003 (t = 0.451 s) and 46978 (t = 0.615 s). It is possible to appreciate the change in elongation from MAST to MAST-U cases.

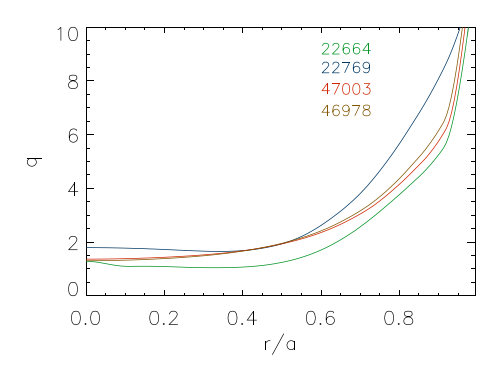


Figure 8. Safety factor profiles for MAST cases 22664 (t = 0.23 s) and 22769 (t = 0.2 s) and MAST-U cases 47003 (t = 0.451 s) and 46978 (t = 0.615 s).

reported in table 1 together with the other main plasma parameters such as plasma current I_p , vacuum toroidal magnetic field on axis B_0 , inverse aspect ratio etc. In figure 9, angular frequency profiles are shown. For the cases #22769 (blue), #47003 (red), #46978 (brown) a low frequency value $f \approx 7 \, \text{kHz}$ has been observed. The case #22664 presents a larger value of frequency $f \approx 24 \, \text{kHz}$ close to the axis and this can help to stabilize the plasma from the point of view of MHD activity. As mentioned in the introduction, the interaction between plasma rotation and stochasticity is an important and complex subject.

The MAST discharges are in L-mode and were produced as part of a collisional scan to test the sensitivity of confinement, and they have been discussed in [5]. These latter together with MAST-U cases have been selected with the goal to explore a certain range of collisionality that represents a good parameter value for the applicability of the stochastic model. The MAST-U cases are in H-mode regime.

⁸ Magnetic stochasticity has been demonstrated to affect plasma rotation in both stellarators [36] and tokamaks with externally imposed resonant magnetic perturbations [37]. The models used in this paper do not include momentum transport. The observed rotation profile is used in the TGLF model to capture the impact of flow shear on drift-wave turbulence.

Table 1. Values of parameters for the MAST shot 22664, 22769 and MAST-U shots 47003, 46978. We report the following quantities: current I_p , vacuum toroidal magnetic field at geometric axis B_0 , Mach number M, auxiliary power P_{NBI} from NBI, q_{95} , Z_{eff} , $\beta = n(\text{Te} + \text{Ti})/[B_0^2/(2\mu_0)]$, elongation κ , inverse aspect ratio $\epsilon = a/R$, H-factor defined as the ratio between the global energy confinement time τ_E and value of τ_E obtained via the IPB98(y, 2) scaling.

Shot number	$I_p(kA)$	B_0 (T)	М	$P_{ m NBI}$	q_{95}	$Z_{ m eff}$	β	κ	ϵ	H_{98}
22664	886	0.50	0.35	3.2	7.2	1.3	0.067	1.73	0.71	1.35
22769	592	0.34	0.32	3.0	9.6	1.3	0.094	1.80	0.7	0.8
47003	730	0.66	0.19	1.3	7.8	1.5	0.051	2.00	0.81	1.34
46978	750	0.60	0.25	3.0	8.5	1.5	0.060	2.15	0.75	1.20

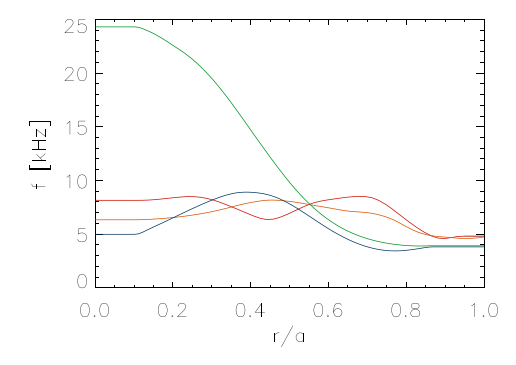


Figure 9. Angular frequency profiles for MAST cases 22664 (t=0.23 s) and 22769 (t=0.2 s) and MAST-U cases 47003 (t=0.451 s) and 46978 (t=0.615 s). The colours associated to shots are the same of figure 8.

6. Results

Here, we describe results of JINTRAC calculations using a variety of stochastic transport models to supplement TGLF (using SAT1 and SAT2) in the JETTO transport solver. In TGLF EM simulations both $B_{||}$ and B_{\perp} were included. MAST-U TGLF calculations were performed with 17 radial points, 2 ion species (D and C) and the following TGLF input file parameters: nbasis_min = 2, nbasis_max = 10, nmodes = 2, $USE_MHD_RULE = F$, kygrid $_$ model = 4, nky = 12, theta_trapped = 0.7, find_width = T, nwidth = 21, nxgrid = 16, width = 1.65, filter = 2.0, $alpha_zf = -1$. The other not specified parameters are set to the default values. The choice of parameter values has been made on the basis of discussions with the TGLF authors [38]. For example, the option alpha_zf = -1 is used to avoid the situation where the saturation rule spuriously finds the lowest k_v mode as the dominant contributor to the flux, another consequence of using TGLF outside its usual domain. Ideally, future improvements to TGLF will include a quasilinear saturation rule developed and tuned specifically for ST turbulence (which is out of scope of this work). Simulations have been performed for the prediction of electron and ion temperature profiles, T_e and T_i , with density and rotation set to fit the experimentally measured profiles, and impurity density profiles estimated using the measured $Z_{\rm eff}$. Our simulations have additionally required as inputs the magnetic equilibrium configuration, and temperatures at the boundary point fixed at r/a = 0.9. Table 2 gives the characteristic mid-radius values of some key plasma parameters from each discharge.

The selected shots span a range in collisionality (indeed the selected MAST discharges are from the extremes of the collisional scan described in [5]), which, as discussed earlier, is an important parameter in the transport processes from stochastic fields.

To make an initial assessment of the possible importance of radial stochastic transport, we can compare magnetic island width, w_i , estimated using equation (1) for a given toroidal mode number, n, with the distance between rational surfaces, $\delta r_{\rm res}$, from equation (2). It is important to note that equation (2) is calculated for a single *n*-mode. Once the complete *n*-spectrum is considered, the distance between adjacent resonant surfaces is lower than $\delta r_{\rm res}$ and consequently stochasticity can occur more easily. The comparison between w_i and $\delta r_{\rm res}$ also requires knowing the amplitude of the magnetic fluctuation, which can be estimated using the Drake ansatz of equation (21). Figure 10 shows this comparison for #22664 for n = 6 and n = 16. We observe that around $r \approx 0.4$ for toroidal number n = 6 (red line), the quantity w_i becomes larger than $\delta r_{\rm res}$ and consequently we expect that stochastic process could become important. By increasing nvalue the threshold stochastic condition shifts toward lower values of r, as shown in figure 10 for n = 16 (blue line). This behaviour is typical in the MAST/MAST-U discharges we have analysed. In particular, for n = 16 we find $w_i > \delta r_{\rm res}$ starting from the position r/a = 0.28, 0.36, 0.26, 0.41 for #47003, #22664, #46798, #22769 respectively.

The ratio between w_i and $\delta r_{\rm res}$ is a good approximation of the so called stochastic parameter. This parameter have been introduced in [80] and could be used to give an estimation of $l_{||c|}$ quantity via the following analytical expression:

$$l_{\parallel c} \approx \frac{\pi R}{\ln\left[\pi w_i / (2\delta r_{\rm res})\right]}.$$
 (27)

It is important to note that equation (27) has been derived for one single n mode [43]. The general expression for a complete spectrum of n is unknown. However, we expect for this case, a value of $l_{\parallel c}$ lower than that one obtained in equation (27). In this paper for MAST/MAST-U we always use n=16 to compute $l_{\parallel c}$, because this is the principal toroidal wave number that emerges in gyrokinetic simulations of MTM turbulence in MAST discharges [26]. It is important to point out that $l_{\parallel c}$ is only weakly sensitive to this choice of n because of the logarithmic dependence in equation (27). To identify the most appropriate reduced stochastic transport model, it is important to consider the collisional regime that is relevant to the

Table 2. Local values of parameters for the MAST shots 22664, 22769 and MAST-U shots 47003, 46978. All the value have been calculated in the middle of the radial domain at r/a = 0.5. We report electron T_e and ion T_i temperatures, density n_e , ion ρ_i and electron ρ_e Larmor radius. Mean free path $\lambda_{\rm mfp}$, electron-ion collisional frequency ν_{ei} and longitudinal decorrelation scale $l_{||c}$ are averaged in the central region 0.45 < r/a < 0.75 of the radial domain.

Shot	T_e [eV]	T_i [eV]	$n_e(10^{19}\mathrm{m}^{-3})$	ρ_i (m)	ρ_e [m]	$\langle \lambda_{\rm mfp} \rangle$ [m]	$\langle \nu_{ei} \rangle [\mathrm{s}^{-1}]$	$\langle l_{ c} \rangle$ (m)
22664	600.0	683.3	3.2	$1.1\cdot 10^{-2}$	$1.6 \cdot 10^{-4}$	8.39	$1.90\cdot 10^6$	2.18
22769	361.6	438.5	3.4	$1.3 \cdot 10^{-2}$	$1.9 \cdot 10^{-4}$	3.07	$4.02 \cdot 10^{6}$	2.89
47003	570.1	616.0	4.7	$7.7 \cdot 10^{-3}$	$1.2 \cdot 10^{-4}$	6.78	$2.10 \cdot 10^6$	4.19
46978	541.8	595.0	4.64	$8.3 \cdot 10^{-3}$	$1.3 \cdot 10^{-4}$	5.81	$2.33 \cdot 10^6$	2.86

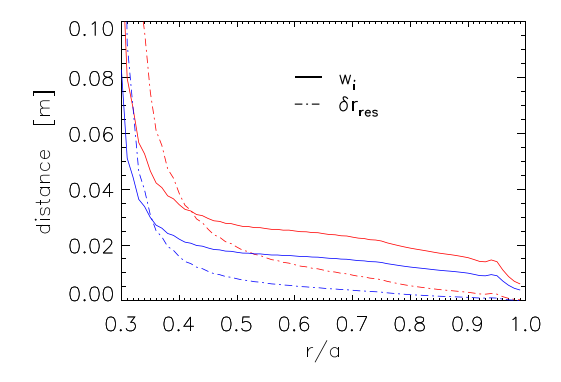


Figure 10. Comparison between magnetic island w_i and distance between rational surfaces $\delta r_{\rm res}$ for n=6 (red lines) and n=16 (blue lines). The curves referred to the 22664 MAST case.

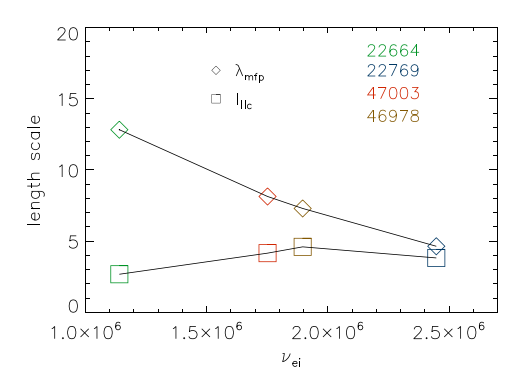


Figure 11. Mean free path λ_{mfp} and $l_{||c|}$ parameters expressed in meters (m) as a function of collisionality ν_{ei} in $[s^{-1}]$.

experimental conditions. In figure 11, we compare the mean free path $\lambda_{\rm mfp}$ and the $l_{||c}$ value calculated in the middle of the radial domain, for each of the four discharges. Both quantities are plotted as a function of the mid-radius collisionality ν_{ei} , which varies across the discharges, and Figure 12 compares radial averages $\langle \lambda_{\rm mfp} \rangle$ and $\langle l_{||c} \rangle$ as functions of $\langle \nu_{ei} \rangle$, where the average is performed over the region 0.45 < r/a < 0.75.

Figures 11 and 12 clearly demonstrate that $\lambda_{\rm mfp} > l_{||c}$ in the lowest collisional MAST discharge #22664, and that this criterion is also satisfied less strongly in MAST-U discharges #47003 and #46978. Satisfying $\lambda_{\rm mfp} > l_{||c}$ indicates that the more suitable RR stochastic model for these discharges will be the 'collisionless' model (see section 3.1). Identifying the appropriate RR collisional regime is more ambiguous for MAST #22769 where $\lambda_{\rm mfp} \approx l_{||c}$. The RR-collisionless

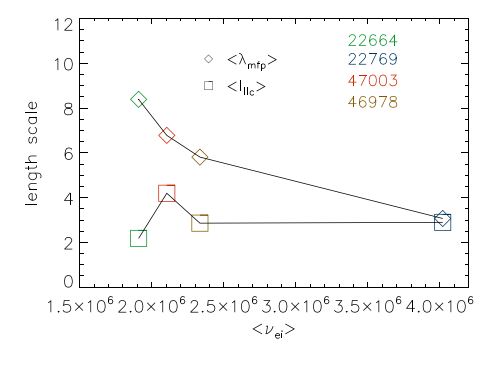


Figure 12. Average mean free path $\langle \lambda_{\rm mfp} \rangle$ and average $\langle l_{||c} \rangle$ parameters expressed in meters (m) as a function of the average collisionality $\langle \nu_{ei} \rangle$ in [s⁻¹]. Quantities are averaged between r=0.45a and r=0.75a.

 RR_{c-less} model has been used in JETTO together with either TGLF(SAT1) or TGLF(SAT2).

6.1. RR and TGLF(SAT1)

Here, we first report transport simulations for the MAST-U H-mode #47003, using the RR_{c-less} model and TGLF(SAT1) excluding further effects from magnetic fluctuations (TGLF(SAT1)ES). The top panel of figure 13 compares T_e and T_i experimental profiles (dash-dotted lines) with the transport steady state profile predictions (continuous lines). The bottom panel shows the total electron and ion thermal diffusivities, χ_e and χ_i , together with their respective contributions from the RR_{c-less} model, and from ion neoclassical heat transport, $\chi_{i_{\rm neo}}$. Ion heat transport is entirely dominated by the neoclassical term #47003, while electron heat transport is dominated by stochasticity, in particular in the central box around r = 0.4 with the peak electron heat diffusivity $\chi_e \sim \chi_{eRR} \sim 3\,\mathrm{m}^2\,\mathrm{s}^{-1}$.

Modelling the same discharge including electromagnetic effects in TGLF ($RR_{c-less}+TGLF(SAT1)EM$) gives the similar temperature profile predictions illustrated in the top panel of figure 14. The bottom panel shows that the small change in profiles is due to the presence of enhanced ion transport between 0.6 < r < 0.8, and comparison with figure 13 indicates that this can be attributed to the inclusion of magnetic fluctuations in TGLF(SAT1)EM⁹.

⁹ The nature of the electromagnetic modes predicted by TGLF EM in this region will be investigated in future work, and may be due to the onset of hybrid-KBMs [81].

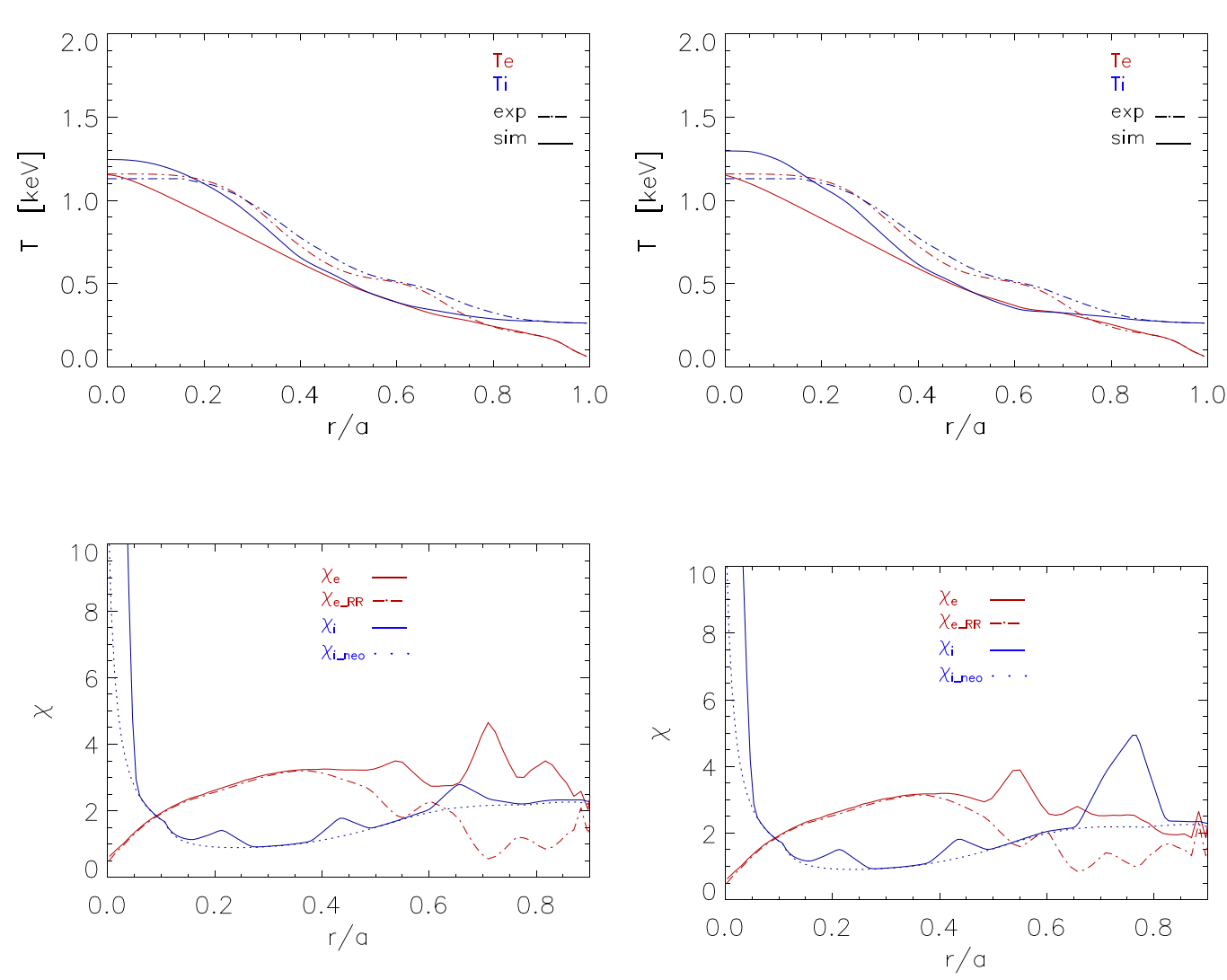


Figure 13. (Top panel) Experimental data (dash-dotted line) of ion and electron temperature profiles compared with simulation profiles (continuous lines) for the MAST-U case 47 003 in electrostatic transport model . (Bottom panel) Associated total ion and electron diffusion coefficient χ_i and χ_e in blue and red continuous lines respectively. Rechester-Rosenbluth $\chi_{\rm RR}$ and neoclassical diffusion $\chi_{i_{\rm neo}}$ coefficients in red dashed and blue dotted lines respectively. Diffusion coefficients are expressed in [m² s⁻¹]. The used model has been the RR_{c-less}+TGLF(SAT1).

Figure 14. (Top panel) Experimental data (dash-dotted line) of ion and electron temperature profiles compared with simulation profiles (continuous lines) for the MAST-U case 47 003 in electromagnetic transport model. (Bottom panel) Associated total ion and electron diffusion coefficients as in figure 13. Diffusion coefficients are expressed in $[m^2 \, s^{-1}]$. The used model has been the $RR_{c-less}+TGLF(SAT1)$.

 $RR_{c-less}+TGLF(SAT1)EM$ transport simulations for MAST-U #46978 give the profile predictions shown in figure 15. The top panel shows that both electron/ion profiles, and especially T_i , are under-predicted. Neoclassical transport, shown in the bottom panel, dominates the ion heat channel across most of the radial profile, and is similar to that in MAST-U #47003. Electron heat transport is lower than the ion heat transport, and is always dominated by stochasticity. Replacing TGLF(SAT1)EM by TGLF(SAT1)ES in the transport calculation results in extremely similar profile predictions, indicating that TGLF(SAT1)EM is not finding significant transport from electromagnetic modes in this discharge.

 $RR_{c-less}+TGLF(SAT1)EM$ transport simulations for MAST #22664 are shown in figure 16. In this discharge the temperature profiles are over-predicted in both channels for

r/a < 0.4. The RR modelled stochastic transport coefficients are notably larger than in both MAST-U H-mode discharges, and $\chi_{e_{\rm RR}}^{e-{\rm less}}$ peaks at a value of 5 m² s⁻¹ around r=0.3. As for #46978, replacing TGLF(SAT1)EM by TGLF(SAT1)ES has minimal impact on the transport steady state profiles, so the significant enhancement of χ_e over $\chi_{e_{\rm RR}}$ at r/a > 0.4 predicted by TGLF can be attributed to electrostatic instabilities; ETG would be a likely candidate. Neoclassical ion heat transport still dominates the ion heat transport channel, but $\chi_{i,\rm neo}$ is rather lower than in the MAST-U discharges.

6.2. RR-hybrid + TGLF(SAT1)EM

For the more ambiguous collisional discharge, #22769, with $\lambda_{\rm mfp} \approx l_{||c}$, we adopt the following RR-hybrid model that

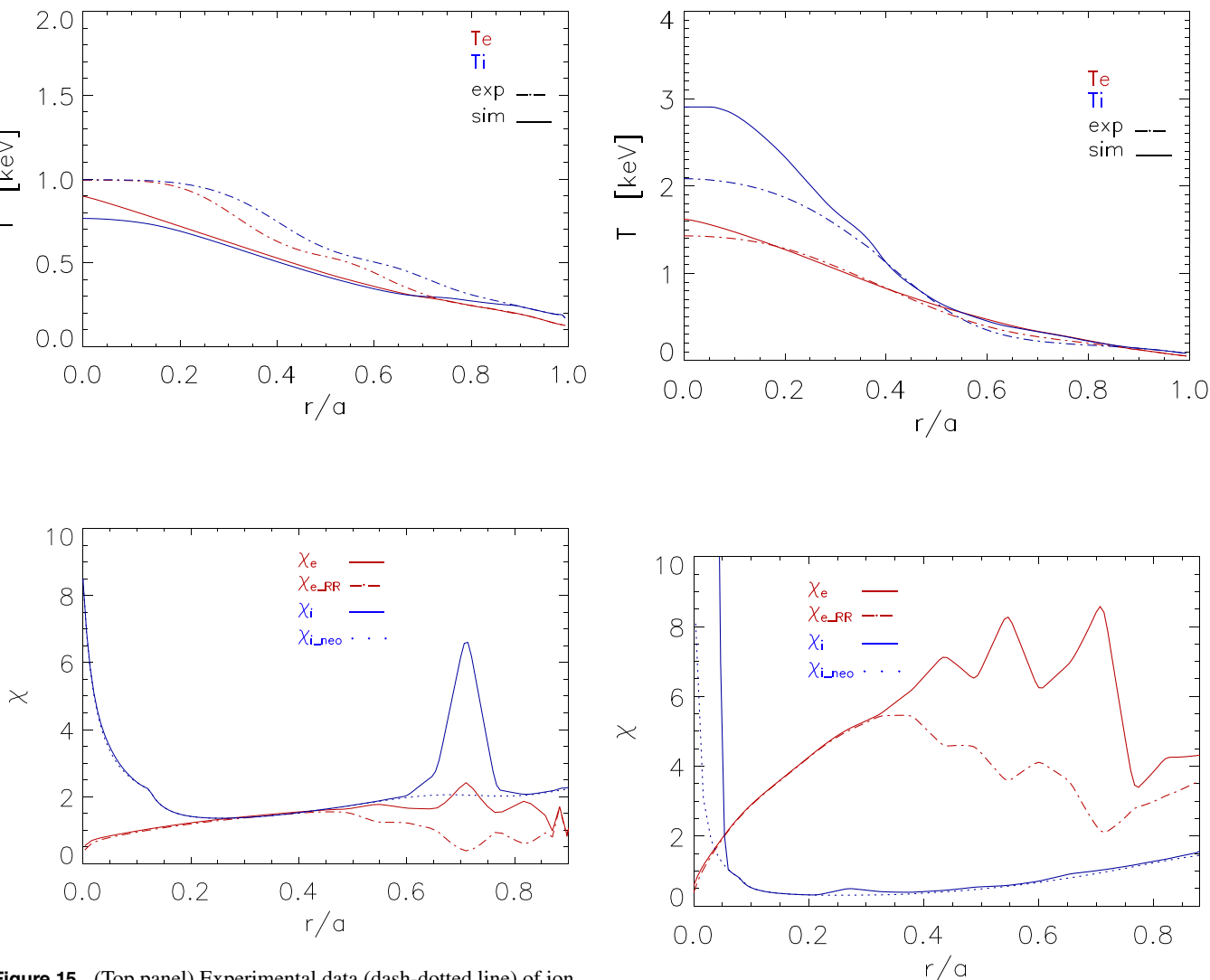


Figure 15. (Top panel) Experimental data (dash-dotted line) of ion and electron temperature profiles compared with simulation profiles (continuous lines) for the MAST-U case 46 978 in electromagnetic transport model. (Bottom panel) Associated total ion and electron diffusion coefficients as in figure 13. Diffusion coefficients are expressed in $[m^2 \, s^{-1}]$. The used model has been the $RR_{c-less}+TGLF(SAT1)$.

should be more appropriate for describing the stochastic transport at transitional collisionality:

$$\chi_{e_{Hy}} = \left(\frac{1}{\chi_{e_{RR_c-less}}} + \frac{1}{\chi_{e_{RR_{coll}}}}\right)^{-1}.$$
(28)

This model combines the RR-collisionless RR_{c-less} and RR-collisional RR_{coll} models, and accounts for collisionality increasing towards the edge because of the reduction in λ_{mfp} . Towards the edge we may expect to find $\lambda_{mfp} < l_{||c}$, which will reduce transport coefficients by a factor $\lambda_{mfp}/l_{||c}$ with respect to the RR_{c-less} model.

Transport calculations using RR-hybrid + TGLF (SAT1)EM for MAST #22769 are shown in figure 17. We note that transport calculations using this model for the other discharges find no substantial differences to the RR-collisionless results presented in figures 14–16. This is because for these

Figure 16. (Top panel) Experimental data (dash-dotted line) of ion and electron temperature profiles compared with simulation profiles (continuous lines) for the MAST-U case 22 664 in electromagnetic transport model. (Bottom panel) Associated total ion and electron diffusion coefficients as in figure 13. Diffusion coefficients are expressed in $[m^2 s^{-1}]$. The used model has been the $RR_{c-less}+TGLF(SAT1)$.

discharges $\lambda_{\rm mfp} > l_{||c}$ at least for $r/a \lesssim 0.9$ after which we impose boundary conditions.

An extension of this hybrid model will be developed in a future work. It is also interesting to note that χ_e and $\chi_{e_{RR}}$ are larger in the two MAST than in the MAST-U that we have examined. This is probably due to the different gradients involved and, as mentioned, to the fact that magnetic field is larger in the two MAST-U cases.

6.3. RR + TGLF(SAT2)EM

Transport calculations using $RR_{c-less} + TGLF$ (SAT2)EM give significantly stronger transport, and flatter profiles: e.g. see transport calculation results for MAST-U #47003 in figure 18. Comparison of these profiles with SAT1 results in figure 13

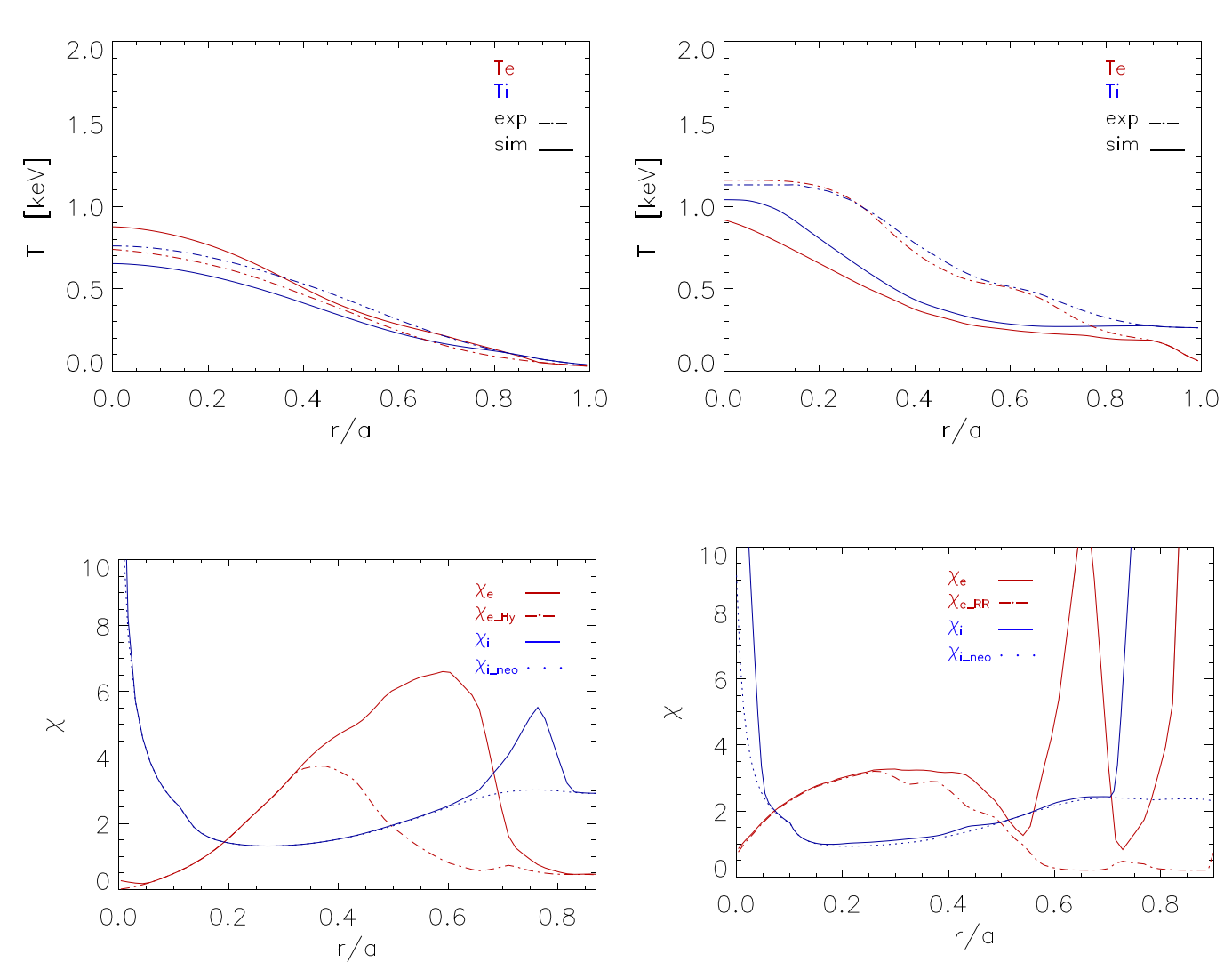


Figure 17. (Top panel) Experimental data (dash-dotted line) of ion and electron temperature profiles compared with simulation profiles (continuous lines) for the MAST case 22 769 in electromagnetic transport model. (Bottom panel) Associated total ion and electron diffusion coefficients as in figure 13. Diffusion coefficients are expressed in $[m^2 \, s^{-1}]$. The used model has been the $RR_{hybrid}+TGLF(SAT1)$.

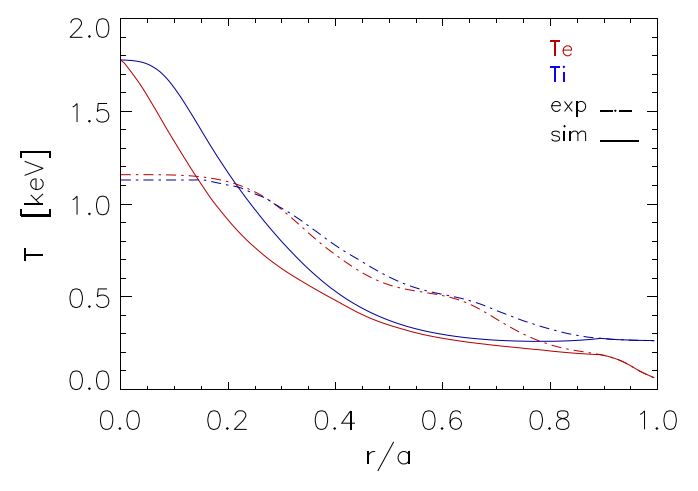
shows that SAT2 gives higher electron (ion) heat diffusivities for r/a > 0.5 (r/a > 0.7). In particular, we observe that SAT2 predicted transport becomes extremely strong in correspondence of flat ion/electron temperature profiles when stochastic diffusivity assumes slow values. This is confirmed by removing flat ion profile and assuming an ion temperature profile with a gradient different from zero in the region r/a > 0.7 (not shown). In this case, it is observed that ion heat diffusivity decreases at values lower than $10\,\mathrm{m}^2\,\mathrm{s}^{-1}$. This represents a clear indication of which points need to be investigated to improve the TGLF(SAT2) model.

6.4. RLW and TGLF(SAT1)EM

Concerning results related to the RLW model, figure 19 shows example transport calculation results using RLW+TGLF(SAT1)EM for MAST-U #47003.

Figure 18. (Top panel) Experimental data (dash-dotted line) of ion and electron temperature profiles compared with simulation profiles (continuous lines) for the MAST-U case 47 003 in electromagnetic transport model. (Bottom panel) Associated total ion and electron diffusion coefficients as in figure 13. Diffusion coefficients are expressed in $[m^2 \, s^{-1}]$. The used model has been the $RR_{c-less}+TGLF(SAT2)$.

Comparing with the experimentally measured profiles, the modelled temperature profiles are much flatter at mid-radius and steeper in the core. The stochastic transport model, $\chi_{e_{RLW}}$, dominates the transport, though its profile is starkly different to that from the other RR stochastic models we have considered: in particular there is an enormous rise in $\chi_{e_{RLW}}$ in the edge plasma, which is absent in $\chi_{e_{RR}}$. This edge enhancement appears in $\chi_{e_{RIW}}$ principally due to the strong edge density gradient in the MAST-U plasma. Reducing the amplitude of the density gradient term in equation (19) would reduce the edge transport. Strong edge density gradients are typical in STs, resulting in RLW model predictions of very large transport when above the critical temperature gradient. The reason for including a density gradient term in a model of stochastic transport in tokamaks is not completely clear, though we note that in [50] the authors replaced L_T with $L = (L_T^{-1} + Ln^{-1})^{-1}$ in a collisional reduced model of stochastic transport and



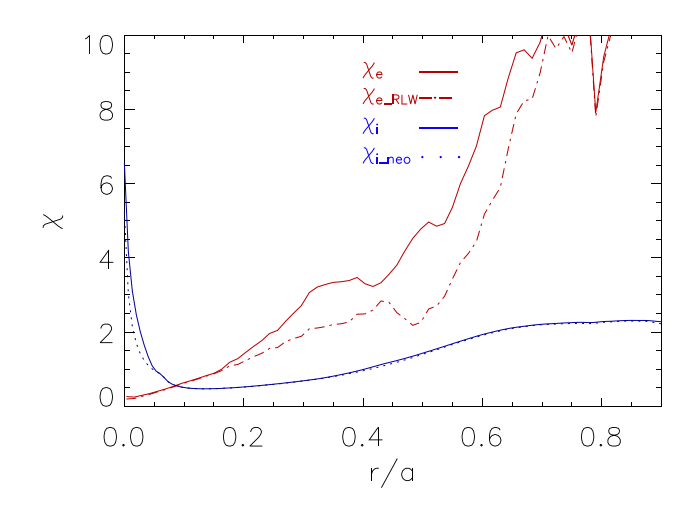


Figure 19. (Top panel) Experimental data (dash-dotted line) of ion and electron temperature profiles compared with simulation profiles (continuous lines) for the MAST-U case 47 003 in electromagnetic transport model. (Bottom panel) Associated total ion and electron diffusion coefficients as in figure 13. The used model has been the RLW + TGLF(SAT1).

found better agreement with the experimental estimate of the electron heat diffusivity from an NSTX H-mode plasma. However, there is no physical explanation for this empirical dependence and further study is needed.

It is also interesting to note from figure 20 that in MAST #22664 the temperature gradient exceeds the RLW critical gradient for the onset of stochastic transport of equation (19) across the whole radial cross-section, and that this has been observed in all the MAST shots we have studied.

As previously mentioned, the RLW model is only sensitive to collisionality, current density and other parameters, via the critical temperature gradient that sets the threshold. Thus the RLW model confinement scalings are insensitive to these quantities for plasmas in MAST, where $|\nabla T_e| > |\nabla T_e|_c$ across the whole plasma. This the RLW model cannot explain the strong favourable energy confinement scaling with collisionality that has been reported by ST experiments [5, 6, 82].

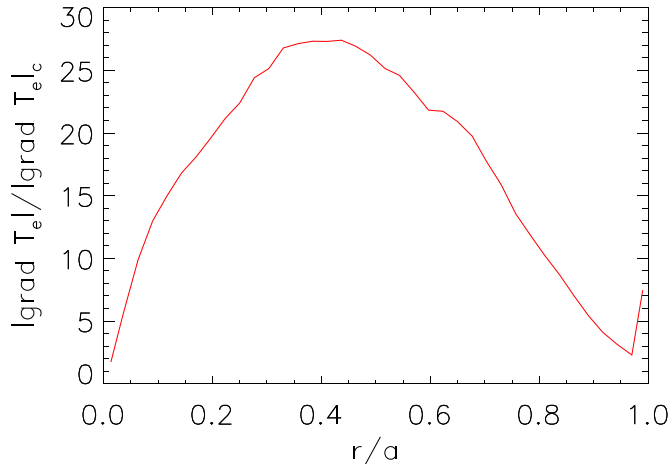


Figure 20. Ratio between temperature gradient and temperature gradient threshold for the case 22 664.

6.5. Summary of model validation

Here we summarise the comparison of MAST and MAST-U experimental profiles against predictions using each of the transport models we have tested. This comparison is quantified for each model prediction by computing the total squared fractional error, χ^2 to measure the quality of agreement with the measured profile.

We briefly summarise the principal characteristics of the method presenting the quantities used for the analysis. If there are x_D profile data $D_{\operatorname{Exp},j}$ to compare with theoretical predictions, to quantify the discrepancy with data $D_{\operatorname{Mod},j}$ of model, we may compute the χ^2 quantity given by:

$$\chi^2 = \sum_{i=1}^{x_D} \frac{(D_{\text{Exp},i} - D_{\text{Mod},i})^2}{D_{\text{Exp},i}^2}.$$
 (29)

The number obtained with this procedure must be compared with the number of degrees of freedom fd that is defined as the number of data points x_D minus the number of free parameters fp in the model. For these cases we have fp = 1. The total squared fractional error per degree of freedom is given by the reduced χ^2 :

$$\bar{\chi}^2 = \frac{\chi^2}{fd} = \frac{\chi^2}{x_D - fp}.$$
 (30)

Reduced $\bar{\chi}^2$ results are shown in figure 21 and in figure 22 for the RR_{c-less}+TGLF(SAT1) and +TGLF(SAT2) respectively and in figure 23 for the RLW + TGLF(SAT1) model.

In this way, we are able to verify if simulation results are sufficiently close to experiments to decide the reliability of models for future predictions. The best values of $\bar{\chi}^2$ have been obtained for the RR_{c-less}+TGLF(SAT1) model. Figures 21 and 22 demonstrate that RR_{c-less}+TGLF(SAT1) and RR_{c-less}+TGLF(SAT2) agree to within $\bar{\chi} < 0.1$ and $\bar{\chi}^2_{\rm max} \approx 0.15$, respectively, of the experimental profiles. It is also clear from figure 23 that there is considerably poorer

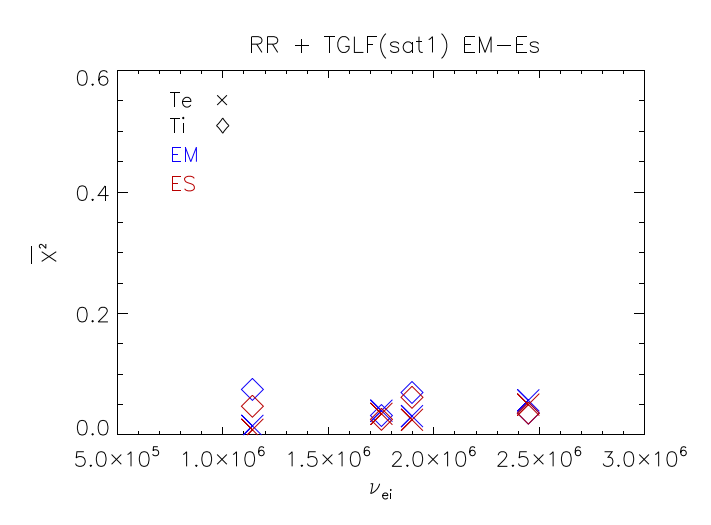


Figure 21. Reduced $\bar{\chi}^2$ as a function of ν_{ei} in $[s^{-1}]$ for predictions obtained with the RR_{c-less}+TGLF(SAT1) model for electrostatic (red) and electromagnetic (blue) regimes.

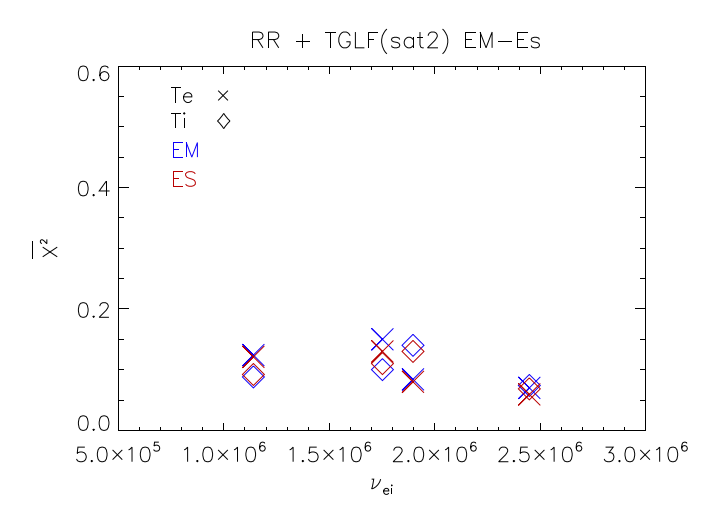


Figure 22. Reduced $\bar{\chi}^2$ as a function of ν_{ei} in [s⁻¹] for predictions obtained with the RR_{c-less}+TGLF(SAT2) model for electrostatic (red) and electromagnetic (blue) regimes.

agreement using RLW+TGLFsat1. Within the level of $\bar{\chi}^2_{\max} \approx 0.10$ and $\bar{\chi}^2_{\max} \approx 0.15$ we can see what is the relative difference in stored energy $W_{e,i} = \int 3/2K_BT_{e,i}ndV$:

$$\Delta W_{e,i} = \frac{W_{e,i_{\text{sims}}} - W_{e,i_{\text{exp}}}}{W_{e,i_{\text{exp}}}}$$
(31)

between experiments and simulations for ions and electrons in the different studied cases.

These quantities are plotted in the histogram of figures 24–26 for RR+TGLF(SAT1), RR+TGLF (SAT2) and RLW+TGLF(SAT1) respectively. Electrostatic and electromagnetic simulations are indicated in red and in blue colours respectively, while ion and electron stored energy quantities are indicated in lighter and darker tones.

In agreement with χ^2 analysis the best results have been obtained for RR+TGLF(SAT1) case at which we can associate a $\Delta W_{i_{\text{max}}} \approx \Delta W_{e_{\text{max}}} \approx 20\%$. Very good results have been obtained for the stored electron energy for the two L-mode

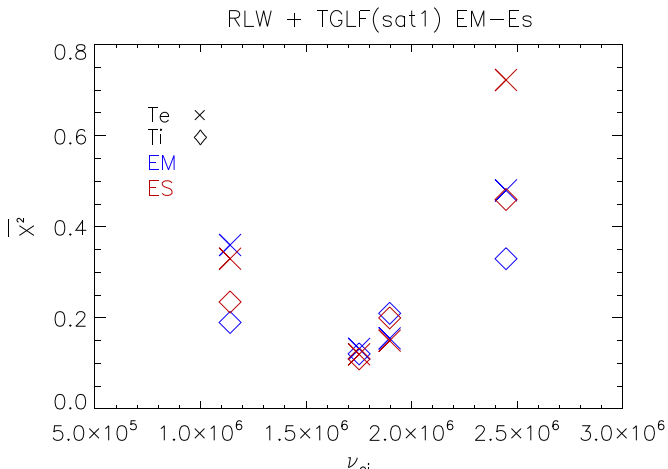


Figure 23. Reduced $\bar{\chi}^2$ as a function of ν_{ei} in $[s^{-1}]$ for predictions obtained with the RLW+TGLF(SAT1) model for electrostatic (red) and electromagnetic (blue) regimes.

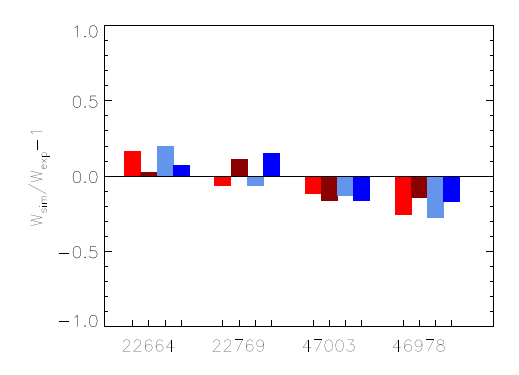


Figure 24. Histogram of stored energy difference $\Delta W_{e,i}$ for the examined shots by adopting the RR+TGLF(SAT1) model. Electrostatic and electromagnetic setup are indicated by using red and blue colour respectively. The lines corresponding to ion and electron are indicated by light and dark colours respectively. Thus from left to right we have the corresponding ion-, electron-electrostatic and ion- and electron-electromagnetic lines.

cases. Moreover, we observe that the best results are related to the RR+ electrostatic TGLF version. The use of the electrostatic version gives slightly better results than electromagnetic version because probably part of EM effects are considered at the same time by reduced stochastic model and by TGLF. These point will be investigated in a future work. However, results obtained by coupling RR+TGLF(SAT1) appear quite promising. Concerning the use of SAT2 we have an energy disagreement $\Delta W_{i_{\max}} \approx \Delta W_{e_{\max}} \approx 40\%$. Good results have been obtained only for the MAST case 22769, but this is only achieved for the total stored energy because radial regions where the simulated pressure exceeds the experimental profile, compensate for regions in which simulation pressure under-predicts the experimental profile. By considering results obtained with the RR+TGLF(SAT1) model, in figure 27 we plot the ratio between the averaged quantities of $X_{e_{RR}}$ and X_e as a function of $\langle \lambda_{mfp} \rangle / \langle l_{||c} \rangle$. The red line is referred to the ratio $\langle X_{e_{RR}} \rangle / \langle X_e \rangle$, whose quantities $\langle X_{e_{RR}} \rangle$ and $\langle X_e \rangle$ are respectively averaged in the central radial region

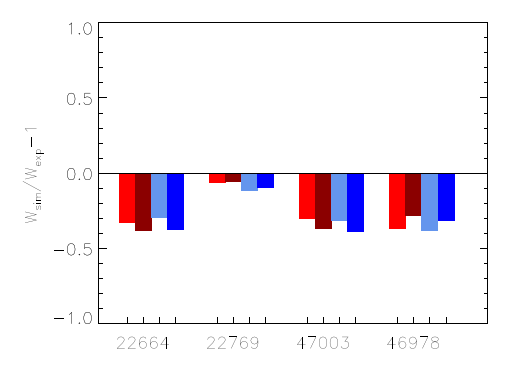


Figure 25. Histogram of stored energy difference $\Delta W_{e,i}$ for the examined shots by adopting the RR+TGLF(SAT2) model. Electrostatic and electromagnetic setup are indicated by using red and blue colour respectively. The lines corresponding to ion and electron are indicated by light and dark colours respectively. Thus, from left to right we have the corresponding ion-, electron-electrostatic and ion- and electron-electromagnetic lines.

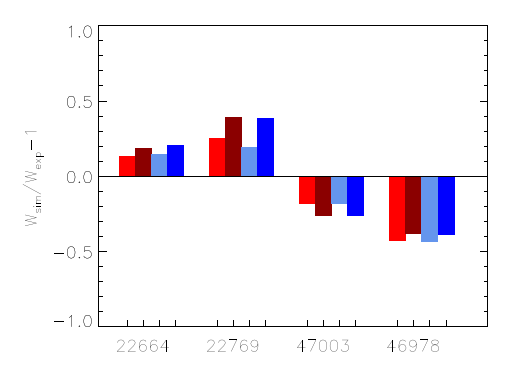


Figure 26. Histogram of stored energy difference $\Delta W_{e,i}$ for the examined shots by adopting the RLW+TGLF(SAT1) model. electrostatic and electromagnetic setup are indicated by using red and blue colour respectively. The lines corresponding to ion and electron are indicated by light and dark colours respectively. Thus from left to right we have the corresponding ion-, electron-electrostatic and ion- and electron-electromagnetic lines.

r/a = [0.45, 0.75] as for $\langle \lambda_{\rm mfp} \rangle$ and $\langle l_{||c} \rangle$. Green line has been obtained by considering average $\langle X_{e_{
m RR}}
angle$ and $\langle X_e
angle$ along the radial direction until to the boundary conditions at r/a =0.9. In this way, it is possible to obtain a trend about the importance of the stochastic transport played in the different scenarios. It emerges that by moving from a more collisional regime in which $\langle \lambda_{\rm mfp} \rangle \approx \langle l_{||c} \rangle$ towards to a collisionless regime in which $\langle \lambda_{\rm mfp} \rangle \gg \langle l_{||c} \rangle$ the stochastic transport importance increases. This suggest the possibility to qualify the role of stochasticity in the different scenarios in tokamaks and in particular in STs via the parameters involved in two important scales represented by $\lambda_{\rm mfp}$ and $l_{||c}$. Thus, this work can be useful in the predictions of ITER scenarios and in the conception of the STEP design. An exhaustive investigation on this latter subject will be developed in a devoted paper.

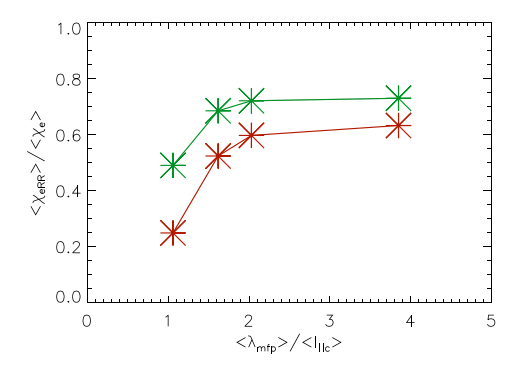


Figure 27. Ratio between averaged quantities of $X_{e_{RR}}$ and X_e as a function of $\langle \lambda_{\rm mfp} \rangle / \langle l_{||c} \rangle$. The red line is referred to the ratio of average $\langle X_{e_{RR}} \rangle$ and $\langle X_e \rangle$ respectively, in the central radial region r/a = [0.45, 0.75], while green line is referred to the ratio of average $\langle X_{e_{RR}} \rangle$ and $\langle X_e \rangle$ along the radial direction until to the boundary conditions at r/a = 0.9.

7. Conclusion

Electromagnetic turbulence is likely to be very important for future plasma regimes, including at high β and in STs, and is therefore of considerable interest to the fusion community. Physics-based reduced models of core transport are essential to improve our capability in integrated scenario modelling for future tokamak plasmas, and these models are less well developed and validated for plasmas where the core turbulence is electromagnetic in character. Microtearing modes, for example, are expected to generate stochastic fields that cause anomalous electron heat transport in such plasmas.

This paper is focussed on testing physics-inspired semiempirical reduced models to describe transport from stochastic fields, and in particular the models developed by Rechester-Rosenbluth and by Rebut-Lallia-Watkins. In the Rechester-Rosenbuth model, the character of the stochastic magnetic field topology must be specified using input parameters, which are prescribed here using formulae involving equilibrium parameters and the expected dominant toroidal mode number, n; the latter is estimated using gyrokinetic simulations of microtearing turbulence in a MAST plasma. The same choice of n is used at all radii and in all of the simulations in this paper. We note that the RR model could likely be improved through more careful estimation of these parameters in different plasma conditions.

In this work we have implemented, in the JINTRAC integrated modelling suite, three reduced models of anomalous electron heat transport from stochastic magnetic fields: RR-collisionless; RR-collisional; and the RLW model. Stochastic field dynamics provide a parallel mechanism for electron heat transport, which complements other transport processes from electrostatic/electromagnetic turbulence that can be described by the TGLF model, and neoclassical transport that can be calculated using NCLASS. Four steady discharges suitable

for transport analysis have been identified from MAST and MAST-U that span a range in parameters including collisionality. We have tested combinations of the stochastic models with TGLF and NCLASS by performing JINTRAC transport simulations for the MAST and MAST-U plasmas. Inspection of the parameters of the MAST and MAST-U plasmas suggests that the RR-collisionless model is the most suitable collisional regime to describe these experiments and STEP. We have also proposed a hybrid variant of the RR model to span collisional regimes. Best transport predictions for the four discharges have been obtained using the RRcollisionless+TGLF(SAT1)ES model. In the framework of the transport, results show a trend for which the importance of the stochasticity with respect to the other electrostatic/electromagnetic instabilities increases by increasing the $\langle \lambda_{\rm mfp} \rangle / \langle l_{||c} \rangle$ ratio. This trend could be very useful in the assessment or qualification of the role of stochasticity in tokamak scenarios. Replacing SAT1 with the SAT2 saturation rule in TGLF renders the predictions less accurate. RLW+TGLF does much less well than the RR+TGLF models, suggesting that the Rechester-Rosenbluth approach more faithfully captures the stochastic transport. To this purpose, we recall that RR model, based on the intuition of the role played by divergence of magnetic field lines in defining stochastic transport, identifies and establishes solid relations between transport and several important length scales that depend on plasma parameters in the regime of interest. Instead, the RLW model, via a parallel between fluids and plasmas, identifies in tokamak a ∇T_c threshold value for stochasticity. In the model, expressions for threshold and for diffusivity have been derived heuristically and mainly on the basis of temperature profiles in JET ohmic plasma scenario. The comparison between these two different approaches to the problem, reveals how the former is probably more general than the second in predicting stochastic transport in different machines. More effort will be required to further improve and more extensively validate reduced transport models for electromagnetic turbulence, either within quasilinear models like TGLF, or by including particle transport, or by complementing its approach as proposed here for stochastic fields using RR-based models.

Data availability statement

All data that support the findings of this study are included within the article (and any supplementary files).

Acknowledgments

Interesting and useful discussions with different people of the MAST-U Team and in particular with S Gibson, E Militello-Asp and M. Valovič are kindly acknowledged. This work has been carried out within the framework of ORB5ST (CINECA) project and has been part-funded by the EPSRC Energy Programme [Grant Number EP/W006839/1]. To obtain further information on the data and models underlying this paper please contact PublicationsManager@ukaea.uk.

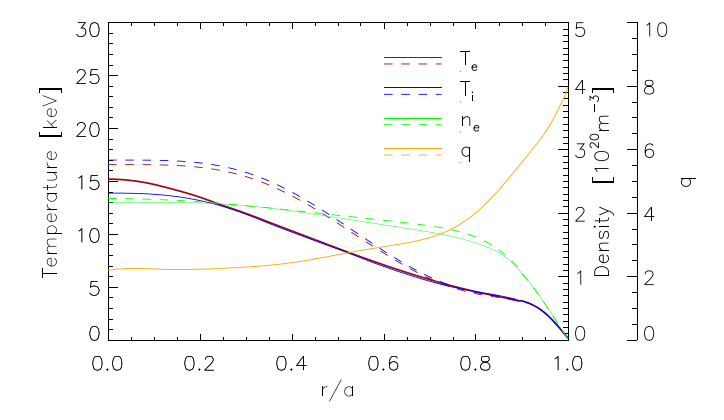
Appendix: Extrapolation to STEP

STEP is a conceptual FPP that aims to achieve a fusion power $P_{\rm fus}=1.56\,{\rm GW}$ in a device with the following principal parameter values: major radius $R=3.6\,{\rm m}$, aspect ratio A=1.8, $B=3.2\,{\rm T}$ and plasma current, $I_p=22.7\,{\rm MA}$ [17]. It is interesting to use the stochastic transport model tested here against MAST and MAST-U, to make a prediction for STEP, noting the obvious caveat that this extrapolation assumes the reduced model tested against MAST/MAST-U also captures the dominant transport in STEP, which will operate in a very different plasma regime.

Reference profiles of density and ion/electron temperatures for a STEP operating point are shown via dashed lines in the top panel of figure 28. From these profiles it is possible to deduce a mean free path $\langle \lambda_{\rm mfp} \rangle \approx 408$ m and a $\langle l_{||c} \rangle \approx 25$ m. These values have been averaged between 0.45 < r/a < 0.75. The quantity $\langle l_{||c} \rangle$ has been calculated for a toroidal number n=16 for which $w_i > \delta r_{\rm res}$ starting from r/a > 0.4. If higher n numbers dominate the toroidal spectrum, a comparison between $\langle \lambda_{\rm mfp} \rangle$ and $\langle l_{||c} \rangle$ indicates that the RR-collisionless model is in the more suitable collisionality regime for predictions.

Preliminary STEP results have been obtained with the $RR_{c-less} + TGLF(SAT1)ES$ model by considering predictive density and ion/electron temperatures (only including D and T ion species). The boundary conditions at the pedestal have been the same adopted in [17]. Predictions are shown by continuous lines in the top panel of figure 28 and the model numerical profiles are not so far from the reference STEP profiles. The corresponding heat conduction coefficients are shown in the bottom panel of figure 28. The bottom panel shows that this transport model predicts a significant electron heat transport contribution from stochastic fields. We observe also a comparable transport determined by ITG instability and a less important transport from ETG instability. In particular, in a STEP configuration we find $\langle \chi_{e_{RR}} \rangle / \langle \chi_e \rangle = 0.7$ and $\langle \chi_{e_{RR}} \rangle / \langle \chi_e \rangle = 0.65$ for average quantities calculated in the central range r/a = [0.45, 0.75] and along the radial direction until boundary conditions respectively. These values are in agreement with the trend obtained in figure 27 according to which moving towards a scenario with $\langle \lambda_{\rm mfp} \rangle \gg \langle l_{||c} \rangle$ the importance of stochasticity increases. At the same time, the maximum value of transport along the radial direction is similar or lower than those of MAST/MAST-U shots. Thus, it can happen that the relative importance of stochasticity with respect to other instabilities increases, but the intensity of transport decreases towards regimes such as STEP.

We note that recent local gyrokinetic simulations for STEP suggest that hybrid-KBM electromagnetic turbulence could dominate the transport and that this carries large fluxes at the reference operating point [28, 81]. First flux-driven transport simulations using a new reduced transport model for h-KBM turbulence, however, suggest the existence of a high performance STEP plasma equilibrium with more suitable transport [83]. Thus, further studies need to be done; and in future work we will investigate whether gyrokinetic simulations support



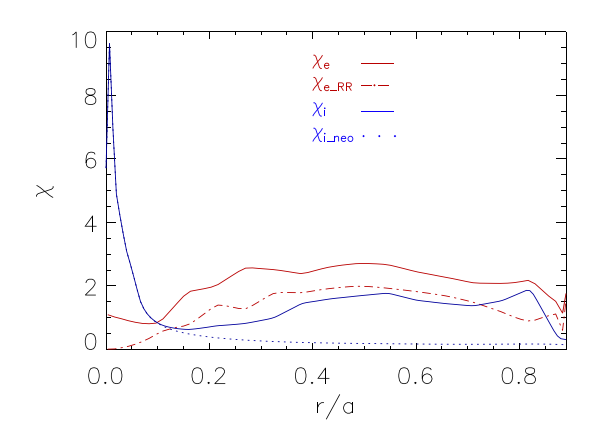


Figure 28. (Top panel) Comparison between design point for STEP and profiles obtained by using $RR_{c-less} + TGLF(SAT1)ES$. (Bottom panel) Transport diffusion coefficient profiles in $[m^2 s^{-1}]$ units.

the existence of regimes in STEP where MTM stochastic transport could be dominant.

ORCID iDs

References

- Spitzer L 1966 Reviews of Plasma Physics vol 2, ed
 M A Leontovich (Consultants Bureau) p 201-297 157
- [2] Sykes A et al 1994 Nucl. Fusion 32 769
- [3] Gerhardt S P et al 2011 Nucl. Fusion 51 073031
- [4] Sabbagh S A et al 2013 Nucl. Fusion 53 104007
- [5] Valovic M et al 2011 Nucl. Fusion **51** 073045
- [6] Kaye S M, Connor J W and Roach C M 2021 Plasma Phys. Control. Fusion 63 123001
- [7] Gryaznevich M et al 1998 Phys. Rev. Lett. 80 3972
- [8] Kaye S M et al 1999 Fusion Technol. **36** 16–37
- [9] Ono M et al 2001 Nucl. Fusion 41 1435
- [10] Gartska G D et al 2003 Phys. Plasmas 10 1805
- [11] Darke A C et al 1995 Fusion Technol. 1 799
- [12] Gusev V K et al 2009 Nucl. Fusion 49 104021

- [13] Minaev V B et al 2018 J. Phys.: Conf. Ser. 1094 012001
- [14] MAST Upgrade Research Plan 2019 *Culham Centre for Fusion Energy* (available at: https://ccfe.ukaea.uk/programmes/mast-upgrade)
- [15] Gryaznevich M and Asunta O 2017 Fusion Eng. Design 123 177
- [16] Berkery J W et al 2024 Nucl. Fusion 64 112004
- [17] Tholerus E et al 2024 Nucl. Fusion **64** 106030
- [18] Roach C M et al 2009 Plasma Phys. Control. Fusion **51** 124020
- [19] Palermo F, Garbet X, Ghizzo A, Cartier-Michaud T, Ghendrih P, Grandgirard V and Sarazin Y 2015 Phys. Plasmas 22 042304
- [20] Palermo F, Garbet X and Ghizzo A 2015 Eur. Phys. J. D 69 8
- [21] Ghizzo A and Palermo F 2015 Phys. Plasmas 22 082303
- [22] Ghizzo A and Palermo F 2015 Phys. Plasmas 22 082304
- [23] Wang W X, Ethier S, Ren Y, Kaye S, Chen J, Startsev E, Lu Z and Li Z Q 2015 Phys. Plasmas 22 102509
- [24] Guttenfelder W, Kaye S M, Kriete D M, Bell R E, Diallo A, LeBlanc B P, McKee G R, Podesta M, Sabbagh S A and Smith D R 2019 Nucl. Fusion 59 056027
- [25] Ren Y et al 2017 Nucl. Fusion 57 072002
- [26] Giacomin M, Dickinson D, Kennedy D, Patel B S and Roach C M 2023 Plasma Phys. Control. Fusion 65 095019
- [27] Guttenfelder W, Candy J, Kaye S M, Nevins W M, Wang E, Bell R E, Hammett G W, LeBlanc B P, Mikkelsen D R and Yuh H 2011 Phys. Rev. Lett. 106 155004
- [28] Giacomin M, Kennedy D, Casson F J, Dickinson D, Patel B S and Roach C M 2024 Plasma Phys. Control. Fusion 66 055010
- [29] Applegate D J, Roach C M, Connor J W, Cowley S C, Dorland W, Hastie R J and Joiner N 2007 Plasma Phys. Control. Fusion 49 1113
- [30] Doerk H, Jenko F, Pueschel M J and Hatch D R 2011 Phys. Rev. Lett. 106 155003
- [31] Dickinson D, Roach C M, Saarelma S, Scannell R, Kirk A and Wilson H R 2012 Phys. Rev. Lett. 108 155003
- [32] Connor J W et al 2006 Proc. 21st IAEA Conf. on Fusion Energy (Chengdu, China, 2006) p TH2/2-2
- [33] Guttenfelder W et al 2012 Phys. Plasmas 19 056119
- [34] Hardman M R et al 2023 Plasma Phys. Control. Fusion **65** 045011
- [35] Patel B S, Hardman M R, Kennedy D, Giacomin M, Dickinson D and Roach C M 2025 Nucl. Fusion 65 026063
- [36] Ida K et al 2015 Nat. Commun. 6 5816
- [37] Unterberg B et al 2007 J. Nucl. Mater. 363 698
- [38] Staebler G M et al 2024 private communication
- [39] Cao M and Diamond P H 2022 Plasma Phys. Control. Fusion 64 035016
- [40] Staebler G M, Kinsey J E and Waltz R E 2007 *Phys. Plasmas* 14 055909
- [41] Staebler G M et al 2008 Proc. 22nd IAEA Fusion Conf. (Geneva, Switzerland) p TH/8-42
- [42] Avdeeva G et al 2023 Nucl. Fusion 63 126020
- [43] Rechester A B and Rosenbluth M N 1979 *Phys. Rev. Lett.* 40 38
- [44] Rechester A B, Rosenbluth M N and White R B 1979 Phys. Rev. Lett. 42 1247
- [45] Rafiq T, Weiland J, Kritz A H, Luo L and Pankin A Y 2016 Phys. Plasmas 23 062507
- [46] Rafiq T, Kaye S, Guttenfelder W, Weiland J, Schuster E, Anderson J and Luo L 2021 Phys. Plasmas 28 022504
- [47] Rebut P H, Lallia P P and Watkins M L 1984 IAEA-CN-50/D-IV-1
- [48] Hamed M, Pueschel M J, Citrin J, Muraglia M, Garbet X and Camenen Y 2023 Phys. Plasmas 30 042303

- [49] Moradi S et al 2020 Phys. Rev. Res. 2 013027
- [50] Wong K L, Kaye S, Mikkelsen D R, Krommes J A, Hill K, Bell R and Leblanc B 2007 2010 Phys. Rev. Lett. Phys. Rev. Lett. 99 135003
- [51] Kaye S M, Guttenfelder W, Bell R E, Gerhardt S P, LeBlanc B P and Maingi R 2014 Phys. Plasmas 21 082510
- [52] Romanelli M et al 2014 Plasma Fusion Res. 9 3403023
- [53] Pereverzev G V et al 1991 ASTRA an automated system for transport analysis IPP Report 5/42 (Max-Planck-Institut fuer Plasmaphysik)
- [54] Drake J F and Lee Y C 1977 Phys. Fluids 20 1341
- [55] Doerk H, Jenko F, Görler T, Told D, Pueschel M J and Hatch D R 2012 Phys. Plasmas 19 055907
- [56] Wesson J 2004 Tokamaks 3rd edn (Clarendon-Oxford)
- [57] Rosenbluth M N and Sagdeev R Z 1984 Handbook of Plasma Physics (North-Holland)
- [58] Kolmogorov A N 1959 Dokl. Akad. Nauk. USSR 98 527
- [59] Farmer J D 1982 Information Dimension and the Probabilistic Structure of Chaos Z. Naturforsh. 37a 1304
- [60] Krommes J A, Oberman C and Kleva R G 1983 J. Plasma Physics 30 56
- [61] Wiesen S et al 2008 JET ITC-Report
- [62] Erba M, Cherubini A, Parail V V, Springmann E and Taroni A 1997 Plasma Phys. Control. Fusion 39 261
- [63] Waltz R E, Staebler G M, Dorland W, Hammett G W, Kotschenreuther M and Konings J A 1997 Phys. Plasmas 4 2482
- [64] Nordman H, Weiland J and Jarmén A 1990 *Nucl. Fusion* 30 983
- [65] Harvey R W, McCoy M G, Hsu J Y and Mirin A A 1981 Phys. Rev. Lett. 47 102
- [66] Nevins W M, Wang E and Candy J 2011 Phys. Rev. Lett. 106 065003
- [67] Doerk H, Challis C, Citrin J, Garcia J, Görler T and Jenko F 2016 Plasma Phys. Control. Fusion 58 115005

- [68] Staebler G M, Candy J, Howard N T and Holland C 2016 Phys. Plasmas 23 062518
- [69] Staebler G M, Belli E A, Candy J, Kinsey J E, Dudding H and Patel B 2021 Nucl. Fusion 61 116007
- [70] Dudding H G, Casson F J, Dickinson D, Patel B S, Roach C M, Belli E A and Staebler G M 2022 Nucl. Fusion 62 0960005
- [71] Baiocchi B, Garcia J, Beurskens M, Bourdelle C, Crisanti F, Giroud C, Hobirk J, Imbeaux F, Nunes I and Contributors J 2015 Plasma Phys. Control. Fusion 57 035003
- [72] McClenaghan J et al 2017 Nucl. Fusion 57 116019
- [73] Pan C et al 2017 Nucl. Fusion 57 036018
- [74] Staebler G M et al 2008 Proc. 22nd IAEA Fusion Conf. (Geneva, Switzerland) p TH/8-42
- [75] Hawryluk R J et al 1980 An empirical approach to tokamak transport Physics of Plasmas Close to Thermonuclear Conditions vol 1, ed B Coppi (CEC) pp 19–46
- [76] Lao L L, St. John H, Stambaugh R D, Kellman A G and Pfeiffer W 1985 Nucl. Fusion 25 1611–22
- [77] Appel L C, Lupelli I 2018 Comp. Phys. Commun.
- [78] Meneghini O, LAO L 2013 Plasma Fusion Res. 8 2403009
- [79] Meneghini O et al 2015 Nucl. Fusion 55 083008
- [80] Zaslavsky V G M and Chirikov B V 1972 Sov. Phys.-Usp. 14 549
- [81] Kennedy D, Giacomin M, Casson F J, Dickinson D, Hornsby W A, Patel B S and Roach C M 2023 Nucl. Fusion 63 126061
- [82] Kaye S M, Gerhardt S, Guttenfelder W, Maingi R, Bell R E, Diallo A, LeBlanc B P and Podesta M 2013 Nucl. Fusion 53 063005
- [83] Giacomin M, Dickinson D, Dorland W, Mandell N R, Bokshi A, Casson F J, Dudding H G, Kennedy D, Patel B S and Roach C M 2025 J. Plasma Phys. 91 E16